484426.

/N - 76-CR

/32-/03

MODELLING DIRECTIONAL SOLIDIFICATION

Progress Report on Grant NAG8-831

1 May 1991 to 31 October 1992

CLARKSON UNIVERSITY

Potsdam, New York 13699-5700

Investigators:

Dr. William R. Wilcox, Dean
    School of Engineering
    (315) 268-6446; fax 3841

Dr. Liya L. Regel, Director
    International Center for Gravity Materials Science
    and Applications
    (315) 268-3841; fax 3841

Graduate student research assistants:

Mr. Jian Zhou, Ph.D. Candidate in Chemical Engineering

Mr. Weijun Yuan, Ph.D. Candidate in Chemical Engineering

S U M M A R Y

Goals and Objectives

The long range goal of this program has been to develop an improved understanding of phenomena of importance to directional solidification, in order to enable explanation and prediction of differences in behavior between solidification on Earth and in space. Current emphasis is on determining the influence of perturbabions on directional solidificaion.

P r o g r e s s

Mr. Zhou completed his M.S. thesis on "Accelerated Crucible Rotation Technique and Current Interface Demarcation during Directional Solidification of Te-doped InSb." Mr. Zhou and Mr. Yuan passed their Ph.D. qualifying examinations.

Professor Liya Regel joined the project as co-investigator. Formerly she was director of the Soviet Academy of Science program on materials processing in space.

The following papers resulted from this project:

1. R. Caram, M. Banan and W.R. Wilcox, "Directional Solidification of Pb-Sn Eutectic with Vibration," J. Crystal Growth 114, 249-254 (1991). (In Appendix A.)

2. M. Banan, R.T. Gray and W.R. Wilcox, "An Experimental Approach to Determine the Heat Transfer Coefficient in Directional Solidification Furnaces," J. Crystal Growth 113, 557-565 (1991). (In Appendix B.)

3. G.T. Neugebauer and W.R. Wilcox, "Experimental Observation of the Influence of Furnace Temperature Profile on Convection and Segregation in the Vertical Bridgman Crystal Growth Technique," Acta Astronautica 25, 357-362 (1991). (In Appendix C.)

4. R.T. Gray and W.R. Wilcox, "Influence of the Accelerated Crucible Rotation Technique on Directional Solidification of InSb-GaSb Alloys," J. Spacecraft & Rockets (submitted). (In Appendix D.)

5. J. Zhou, M. Larrousse, W.R. Wilcox and L.L. Regel, "Directional Solidification with ACRT," J. Crystal Growth (in press).

The following papers were presented at meetings and conferences:

1. J. Zhou, M. Banan, R. Gray and W.R. Wilcox, "Use of Current Interface Demarcation During Directional Solidification of Te-Doped InSb with ACRT," Third Canadian Materials Science Conference, Kingston (June 1991).

2. W.R. Wilcox, "Gravitational Effects on Directional Solidification of Indium Antimonide and Indium Gallium Antimonide," University of Colorado, Boulder (August 1991).

3. J. Zhou, M. Banan, R. Gray and W.R. Wilcox, "ACRT Striations and the use of Current Interface Demarcation during Directional Solidification of Te-doped InSb," Fourth Eastern Regional Conference on Crystal Growth (ACCG/East-4), Atlantic City (October 1991).

4. R. Gray, M. Banan, J. Zhou, M. Larrousse and W.R. Wilcox, "Influence of Perturbations on Directional Solidification of InSb-GaSb Alloy Semiconductors," AIAA, Reno (January 1992).

5. J. Zhou, M. Larrousse and W.R. Wilcox, "Directional Solidification with ACRT," ICCG-10 (August 1992).

6. J. Zhou, M. Larrousse and W.R. Wilcox, "Directional Solidification with ACRT," ICCG-10 (August 1992).

During this reporting period Current Interface Demarcation was used during directional solidification of InSb with Accelerated Crucible Rotation and with vibration. With ACRT, the freezing rate decreased when the ampoule rotation was turned on, and increased when the ampoule rotation was turned off. The total number of striations during each spin-up and spin-down period was one or two less than the number of the current pulses, suggesting that backmelting occurred during ACRT. ACRT had a negligible effect on the interface shape.

The number of grain boundaries in directionally solidified InSb was decreased by the application of vibration and the number of twins was increased, especially at the first-to-freeze part of the ingots.

The quenched interface demarcation technique was used to reveal the interface shape and growth rate during directional solidification of InSb-GaSb alloys. Axial vibration of the ampoule did not seem to affect the average growth rate, but did increase the interface depth during the last-to-freeze parts of the ingots. Vibration appeared to decrease the number of curved boundaries, and to increase the number of straight boundaries.

Future Work

Future work will be the following:

1. More solidification of InSb with both ACRT and CID. One inch diameter ingots will be used in order for the ACRT to generate larger effects.

2. Solidification of doped CdTe with ACRT. Hopefully, we can demarcate the interface.

3. Determine the change of interface shape and position caused by applying vibration during solidification of InSb.

4. Measure the temperature change near the interface caused by vibration.

5. Use a transparent liquid to reveal the flow pattern induced by vibration in a vertical Bridgman configuration.

Directional Solidification with ACRT

Jian Zhou

Summary

The objective of this project is to understand the effect of Accelerated Crucible Rotation Technique (ACRT) on directional solidification of semiconductor alloys. Particularly, we want to determine the variation of freezing rate and solid-melt interface shape caused by use of ACRT during directional solidification. Ingots of Te-doped InSb were solidified with and without ACRT using the vertical Bridgman-Stockbarger technique. Spin-up from rest and spin-down to rest of the growth ampoule was used for ACRT, with a rotation rate of 80 rpm. The rotation on-time ranged from 10 to 40 seconds while the rotation off-time ranged from 10 to 180 seconds. On-time and off-time were sometimes the same and sometimes different. Current Interface Demarcation (CID) was used during solidification. The DC current density was 15.7 amp/cm^2 with a duration of 0.1s and a frequency of 2 hz.

Current and ACRT-induced striations showed that the freezing rate varied during ACRT. The freezing rate decreased when the ampoule rotation was turned on, and increased when the ampoule rotation was turned off. The total number of striations during each spin-up and spin-down period was one or two less than the number of the current pulses, suggesting that backmelting occurred during ACRT.

ACRT had a negligible effect on the interface shape.

Introduction

The major problems in alloy crystal growth are compositional inhomogeneity and polycrystallinity. Two of the reasons for these problems include compositional segregation and time-dependent free convection during solidification. Compositional segregation causes compositional variations in grown crystals. Segregation can also cause constitutional supercooling, which leads to interface breakdown and polycrystallinity. Free convection changes the thermal and compositional field in the melt and may cause fluctuations in the growth rate and compositional inhomogeneities. Striations may develop in the crystals.

The Accelerated Crucible Rotation Technique (ACRT), also known as spin-up and spin-down of the growth ampoule, has been used to overwhelm free convection during crystal growth. Periodic acceleration and deceleration of the crucible rotation leads to effective stirring of the melt, improving compositional homogeneity of crystals [1-4]. Forced convection, the Ekman flow induced by ACRT, changes the heat transfer to the interface from the melt. The consequent change of the temperature field changes the interface shape and may also result in backmelting and regrowth during directional solidification. In these ways it is thought that ACRT may influence the grain size of the resulting ingots.

Current Interface Demarcation (CID) is performed by passing pulses of electric current through the solid-liquid interface during crystal growth [5, 6]. The Peltier effect at the solid-liquid interface changes the interface velocity, thereby creating compositional striations. These striations may be used to indicate the interface position and shape during crystal growth. They also can be used to measure the average growth rate over a short time period.

In this project, we are trying to determine the influence of ACRT on crystal growth of Te-doped InSb by applying CID. Previously we reported that we had finished several runs with CID alone and with ACRT alone, but none with CID and ACRT together. A chemical etching method had been determined to reveal striations. We found that the freezing rate was generally larger than the ampoule translation rate. Turning on and off the ampoule rotation resulted in two compositional striations. The lengths of the material grown during spin-up and during spin-down were different, indicating that the average growth rates during spin-up and spin-down were different. During the period of the present report, we performed several experiments with ACRT alone and found that the average growth rate during spin-up was lower than spin-down by 25 to 50%. We also performed several runs with both ACRT and CID. The growth rate was significantly reduced by turning on the ampoule rotation. The growth rate increased when the ampoule rotation was turned off.

Experimental Methods

Table 1 is a list of the experimental conditions. A detailed description of experimental procedures is given in reference [7]. Two sets of solidification experiments were completed in this period. One set ACRT alone was used, and the other used both ACRT and CID. In the runs with ACRT alone, rotation of the ampoule was applied according to the program shown in Figure 1. The rotation rate was impulsively changed from 0 rpm to 80 rpm and held there for a time. The rotation was then stopped and held at 0 rpm for the same time. After every 10 ACRT cycles, the ampoule rotation was stopped for 3 minutes. The time t was 10 seconds for experiment R3 and was 20 seconds for experiments R8 and R9.

In the runs with both ACRT and CID, high frequency current pulses were applied during the spin-up and spin-down of the ampoule to create several CID striations within each ACRT cycle. Rotation of the ampoule and the current pulses were applied according to the program shown in Figure 2.

After solidification, the ingots were sliced longitudinally along the center. One-half of each ingot was then cut into 25 mm long sections. To reveal the microstructure and striations, the samples were chemically etched in HNO_3-HF-CH_3COOH-Br_2 (100:75:60:2 in volume) for 6 seconds and then in 0.05 M $KMnO_4$-HF-CH_3COOH (1:1:1 in volume) for 6 seconds. After etching, the ingot was viewed using polarized light with a 1/4-wave plate in a Nikon Optiphot-2 microscope.

Results

As mentioned above, we learned that the average growth rates were different during spin-up and spin-down. In order to ascertain whether spin-up caused a larger or smaller freezing rate than spin-down, a computer controlled ACRT program was used. The program used 20 seconds for the regular spin-up and spin-down times. During every 10th ACRT cycle, a longer period (3 minutes) was used for spin-down. By using this program, many sets of striations were obtained. Each set consisted of ten striations for spin-up and nine striations for spin-down, starting with spin-up striations. One set of these striations is shown in Figure 3.

Since we knew the time at which each striation was produced, the average growth rate during each spin-up and spin-down cycle could be measured. The result is shown in Figure 4. For a rotation rate of 80 rpm with 20-second spin-up and 20-second spin-down, the

average growth rate during spin-down was about 25\% higher than during spin-up. For the same rotation rate with 10-second spin-up and 10-second spin down, the average growth rate during spin-down was about 50\% higher than during spin-up, as shown in Figure 5. The lower average growth rate during spin-up suggests that heat transfer from the melt to the interface was enhanced by spin-up.

Figure 4 and Figure 5 show that the average growth rate during 10 second spin-down was almost the same as that during 20 second spin-down. However, the average growth rate during 10 second spin-up was much lower than that during 20 second spin-up. The average growth rate during 10 second spin-up was reduced to the same value as the ampoule translation rate. The more significant reduction of the growth rate during 10 second spin-up suggests that heat transfer was enhanced more during the earlier part of spin-up. Notice that the growth conditions were identical in these two experiments, except for the different ACRT cycle time. In addition, the growth rate data were taken at the middle portion of both ingots, where the ampoule end effect was relatively small and the overall growth rate was relatively constant.

The striations induced by ACRT showed that the solid-melt interface was concave. The interface depth (center-to-edge variation in height) was about the same with or without ACRT. Gray [8] found a similar result during InGaSb solidification with ACRT. He found that ACRT reduced the interface depth to about 0.3 mm from 0.6mm without ACRT. On the other hand, the improvement of the interface shape reported by Capper et al. [3] was remarkable during their VBS solidification of CdHgTe with ACRT. The interface depth was reduced from ~4 mm without ACRT to 1 mm with ACRT. Gray [8] explained that during growth of CdHgTe, heavier HgTe is rejected from the interface and forms a mercury-enriched pool, further increasing the concavity of the interface. ACRT mixes the melt, thereby reducing its concavity even more than the change in heat transfer alone would.

Variation of the freezing rate during ACRT caused compositional striations in the crystals, even without CID. Passage of DC current pulses superimposed current-induced striations on the ACRT-induced striations. Figure 6 shows the surface of a Te-doped InSb ingot solidified with both ACRT and CID. One can see three different types of striations, indicated by A, B, and C. The fine striations labeled A were generated by current pulses. The striations labeled B were caused by starting the ampoule rotation. The striations labeled C were caused by stopping the ampoule rotation. The B striations were wide and had clear edges. The C striations were visible due to the drastic spacing increase of the A striations when ampoule rotation was turned off.

The number of striations in each ACRT cycle was 64-65; one or two striations were missing comparing to the 66 current pulses applied. There are two mechanisms that could account for the missing

striations. The first is that a number of striations could have been removed by backmelting. The second is that during a "no-growth" period, current pulses did not generate any striations. (A "no-growth" period is defined as a time during which the interface velocity is so low that separate striations either cannot form or cannot be revealed by our etching technique.)

In order to determine the variation in freezing rate during each ACRT cycle, the distance between each pair of striations was measured. The growth rate versus time during several ACRT cycles is plotted in Figure 7. The scatter in the data mainly came from errors in the measurement of the distance between striations. The measurement was done at a magnification of 7700x, under which the edges of the striations became curved, resulting in an error of about 15%. The plots show that the growth rate varied almost sinusoidally during ACRT, except at the initial stage of spin-up and spin-down. When the ampoule rotation was turned on, the growth rate decreased rapidly to reach a minimum. When the ampoule rotation was turned off, the growth rate increased rapidly to reach a maximum.

The variation of the growth rate can be understood with knowledge of the interfacial heat transfer during ACRT [9, 10]. First consider the case where heat transfer throughout the system remains constant. The interface position relative to the furnace remains fixed and the freezing rate equals the ampoule translation rate.

When ampoule rotation is turned on, the heat flux from the melt to the interface increases due to enhanced convection. The increased heat flux alters the temperature distribution and forces the interface to move down. While the interface is moving downward, the freezing rate is lower than the ampoule translation rate. If the heat transfer enhancement is large enough, downward movement of the interface overcomes the ampoule translation rate and backmelting occurs.

As ampoule rotation is continued, the downward movement of the interface gradually declines, and the freezing rate approaches the ampoule translation rate. If the ampoule rotation is continued for a sufficiently long time that all of the melt is rotating, heat transfer falls, the interface moves back up, and the freezing rate is below the ampoule translation rate.

If the ampoule rotation is not continued for a sufficiently long time to spin up the entire melt, then stopping the ampoule rotation can also cause the heat transfer to the melt to fall due to formation of a stagnation vortex. This heat flux reduction forces the interface to move upward, resulting in an increase of growth rate above the ampoule translation rate.

8

Future Work

Future work will be focused on the following two sets of experiments:

1. More solidification of InSb with both ACRT and CID. One inch diameter ingots will be used in order for the ACRT to generate larger effects.

2. Solidification of doped CdTe with ACRT. Hopefully, we can demarcate the interface.

References

[1] P. Capper, W.G. Coates, C.L. Jones, J.J. Gosney, C.K. Ard and I. Kenworthy, J. Crystal Growth 83, 69-76 (1987).

[2] P. Capper, J.C. Brice, C.L. Jones, W.G. Coates, J.J.G. Gosney, C. Ard and I. Kenworthy, J. Crystal Growth 89, 171-176 (1988).

[3] W.G. Coates, P. Capper, C.L. Jones, J.J.G. Gosney, C.K. Ard and I. Kenworthy, J. Crystal Growth 94, 959-966 (1989).

[4] P. Capper, W.G. Coates, C.L. Jones, J.J.G. Gosney, I. Kenworthy and C.K. Ard, J. Crystal Growth 102, 848-856 (1990).

[5] M. Lichtensteiger, A.F. Witt and H.C. Gatos, J. Electrochem. Soc. 118, 1013 (1968.

[6] M.J. Wargo and A.F. Witt, J. Crystal Growth 66, 289-298 (1984).

[7] J. Zhou, M.S. Thesis, Clarkson University (1992).

[8] R.T. Gray, PhD Thesis, Clarkson University (1991).

[9] M.F. Larrousse, PhD Thesis, Clarkson University (1987).

[10] M.F. Larrousse and W.R. Wilcox, Chemical Eng. Science 45, 1571-1581 (1990).

Table 1. Experimental Conditions

	R3	R8	R9	RP2	RP3	RP6
ACRT on-time	10 seconds	20 seconds	20 seconds	180 seconds	10 seconds	20 seconds
ACRT off-time	10 seconds	20 seconds	20 seconds	180 seconds	10 seconds	20 seconds
Current Duration	None	None	None	0.05 second	0.05 second	0.1 second
Current Frequency	None	None	None	0.0167 hz	0.0167 hz	1.67 hz
Pull Rate	9.8 mm/hr	10.2 mm/hr	9.7 mm/hr	9.7 mm/hr	10.9 mm/hr	11.5 mm/hr
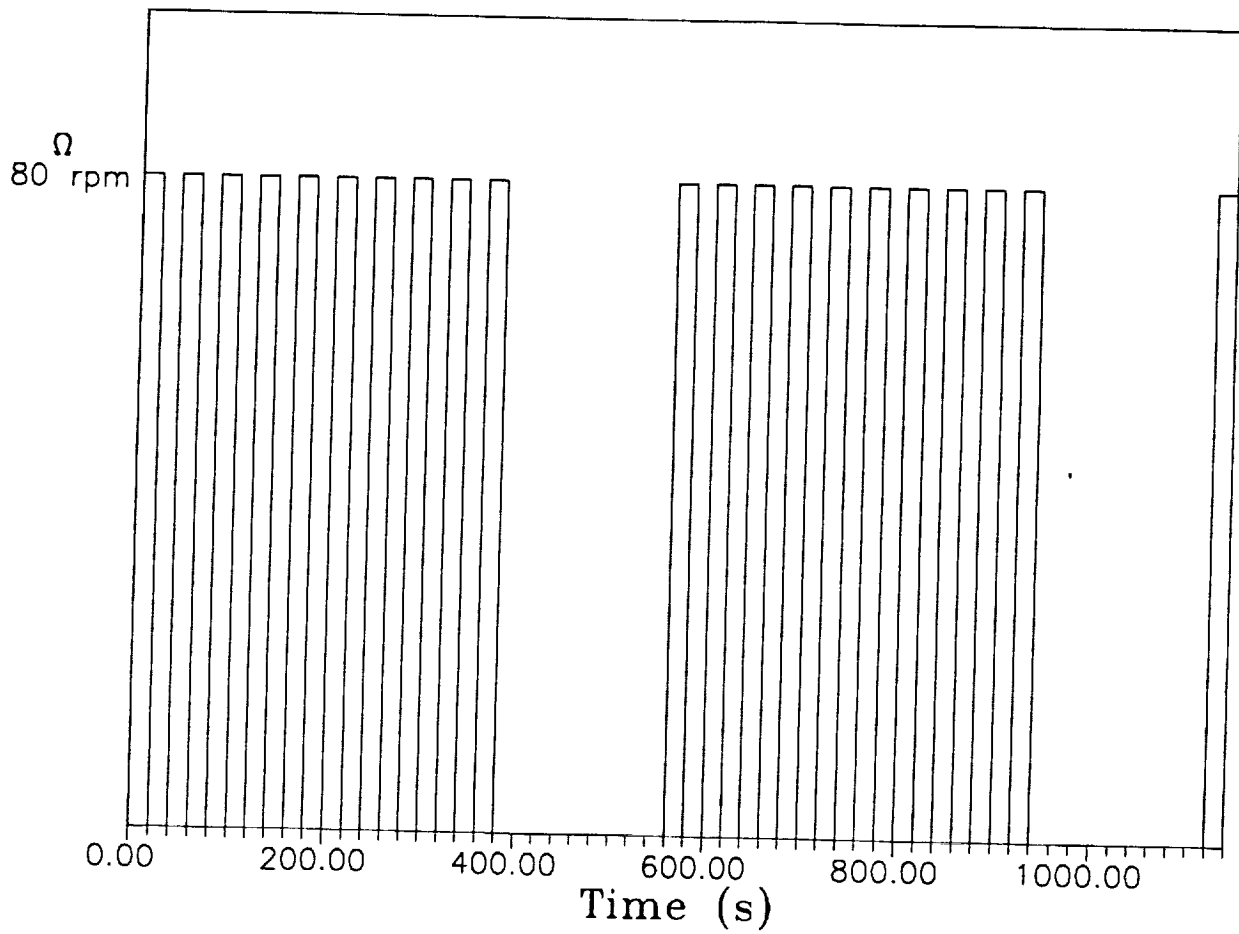
Figure 1. A rotation program used for ACRT.

11
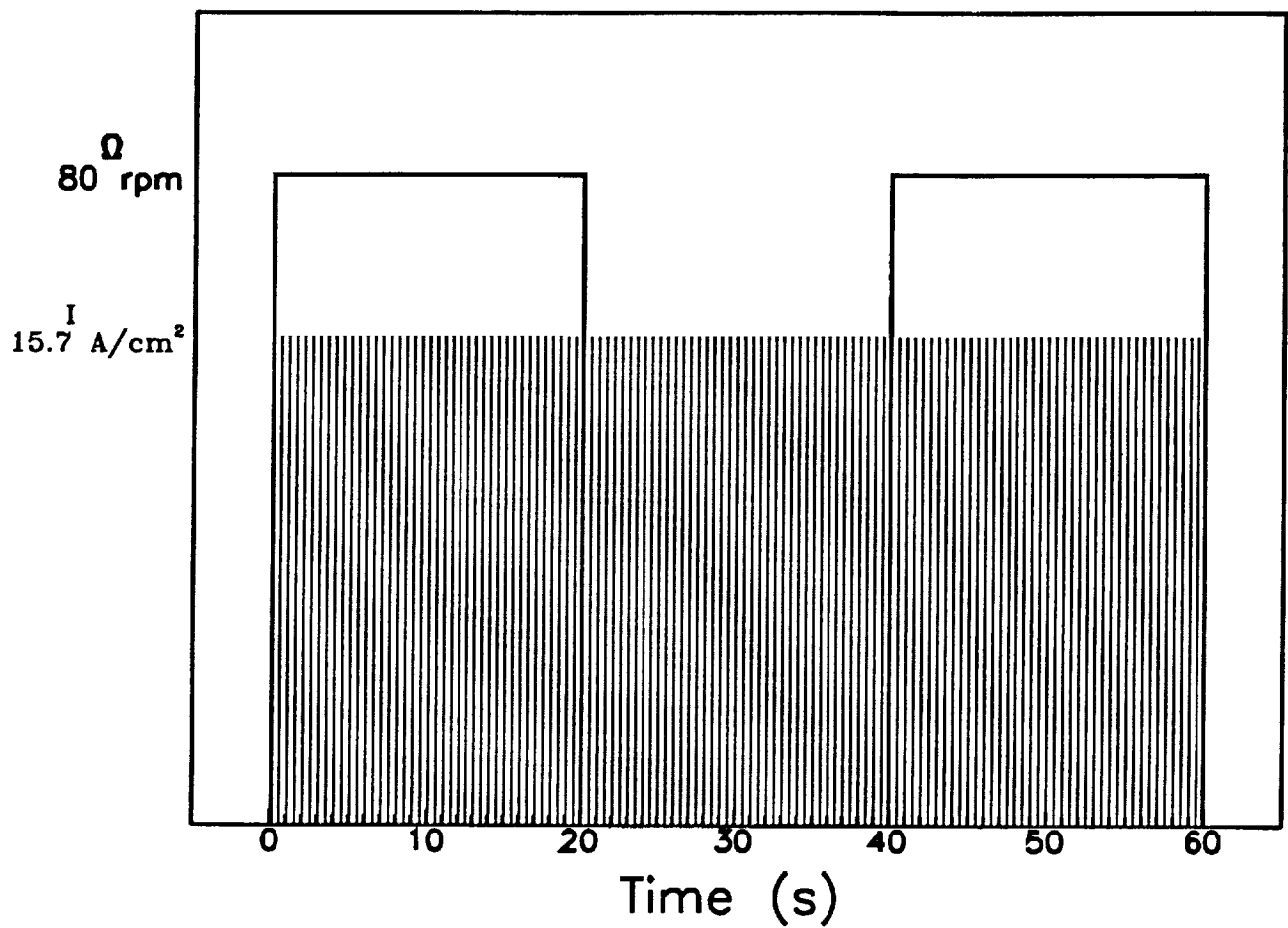
Figure 2. A program for current pulses and ampoule rotation.
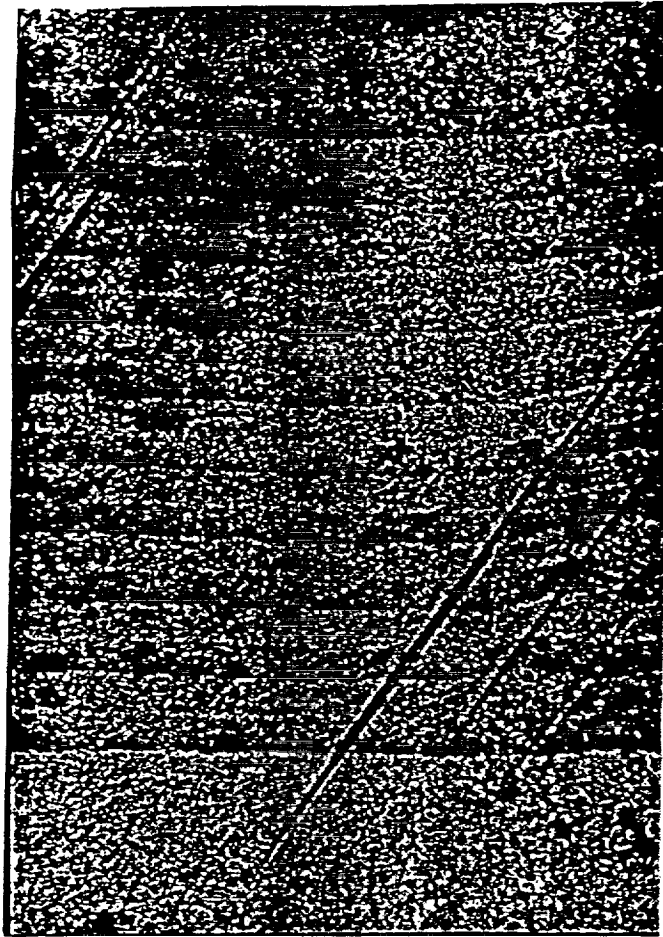
200μm

Figure 3. Photograph of one set of ACRT striations in ingot R8. The first striation was generated by spin-up, the second one by spin-down, etc. The widths of the spin-up striations are smaller than those of the spin-down striations. The growth direction was upward.
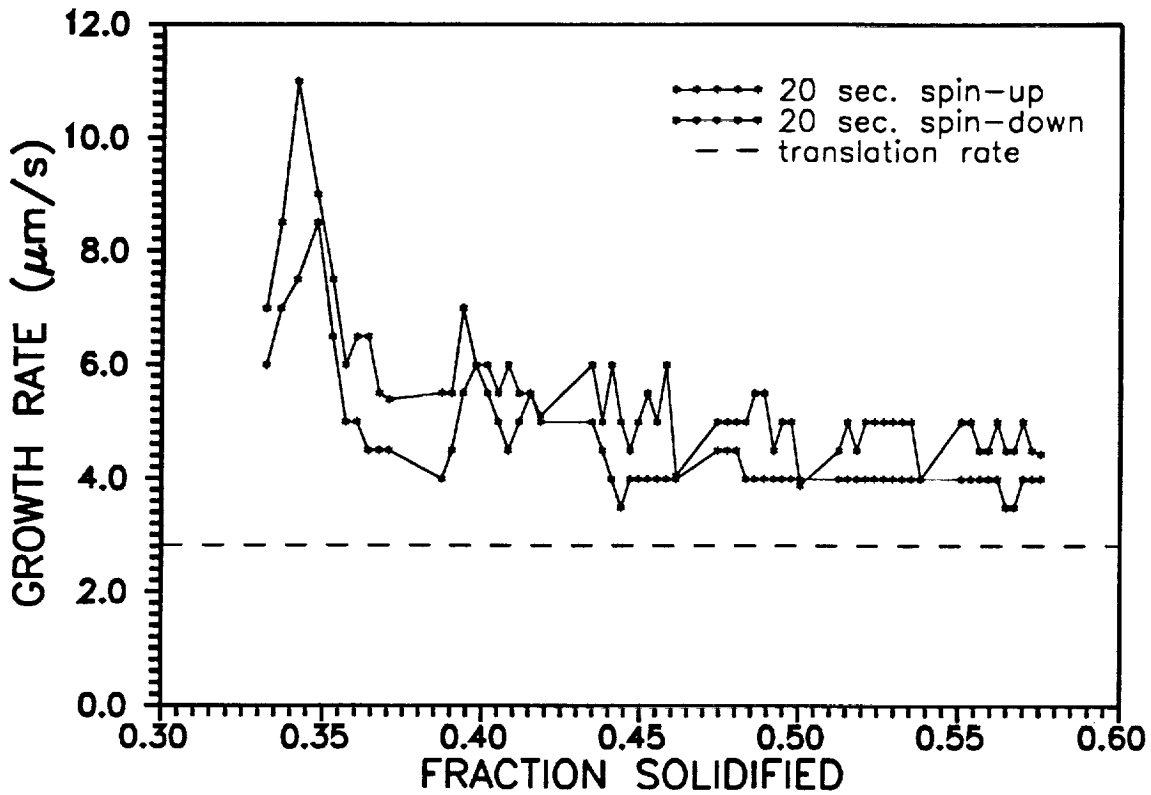
Figure 4. Average growth rate versus fraction solidified during
solidification R8. The ampoule rotation rate was 80 rpm.
Each point represents the average growth rate over 20
seconds of spin-up or 20 seconds of spin-down. The
average growth rate during spin-up was about 25% lower
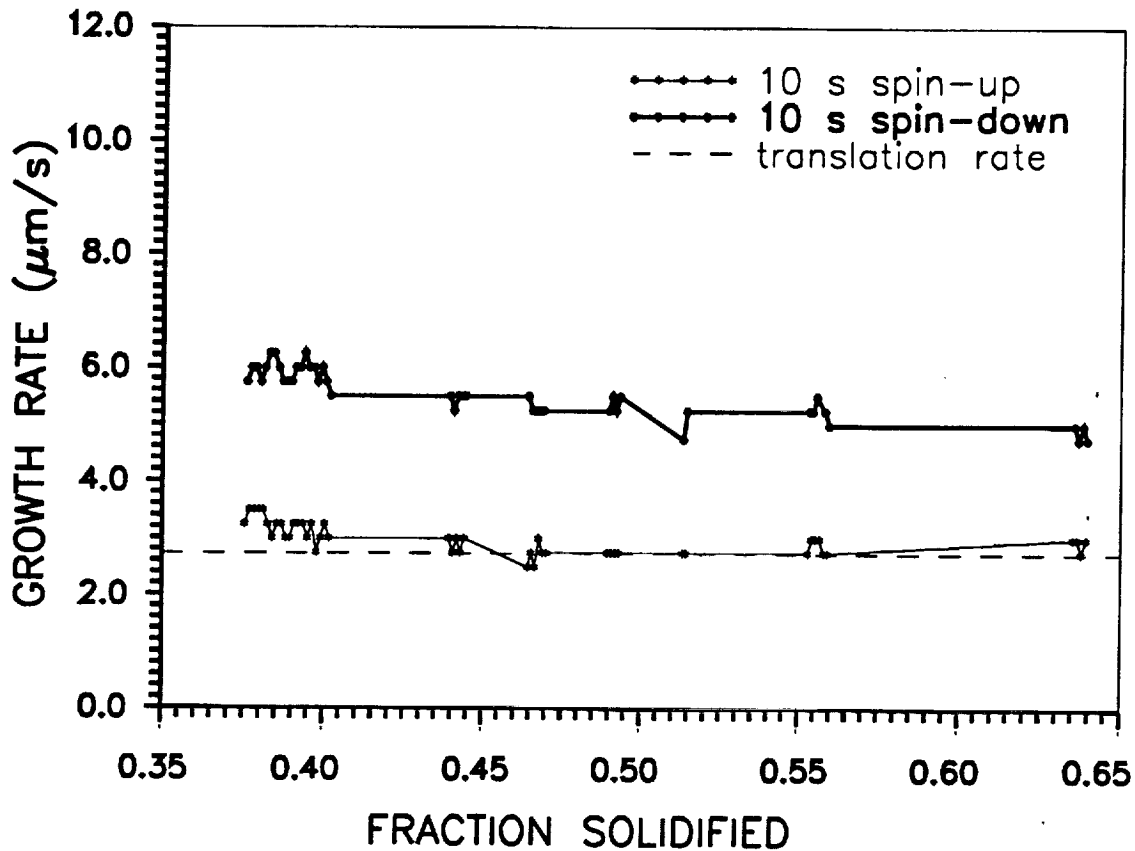than during spin-down.

Figure 5. Average growth rate versus fraction solidified during solidification R3. The ampoule rotation rate was 80 rpm. Each point represents the average growth rate during 10 seconds of spin-up or 10 seconds of spin-down. The average growth rate during spin-up was about 50% lower than during spin-down.
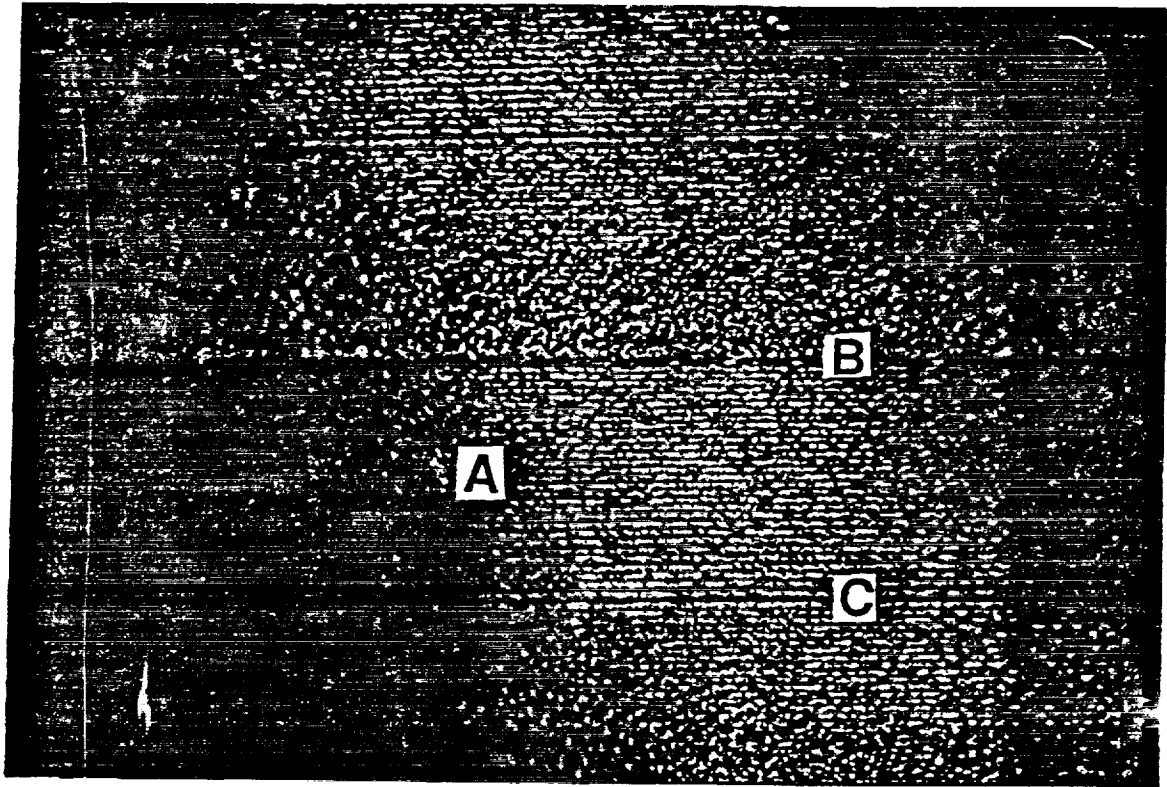
25μm

Figure 6. Photograph of ingot RP6 showing CID and ACRT striations. The fine striations labeled A were generated by current pulses. The striations labeled B were caused by the start of ampoule rotation, and the striations labeled C were caused by stopping ampoule rotation. The growth direction was upward.
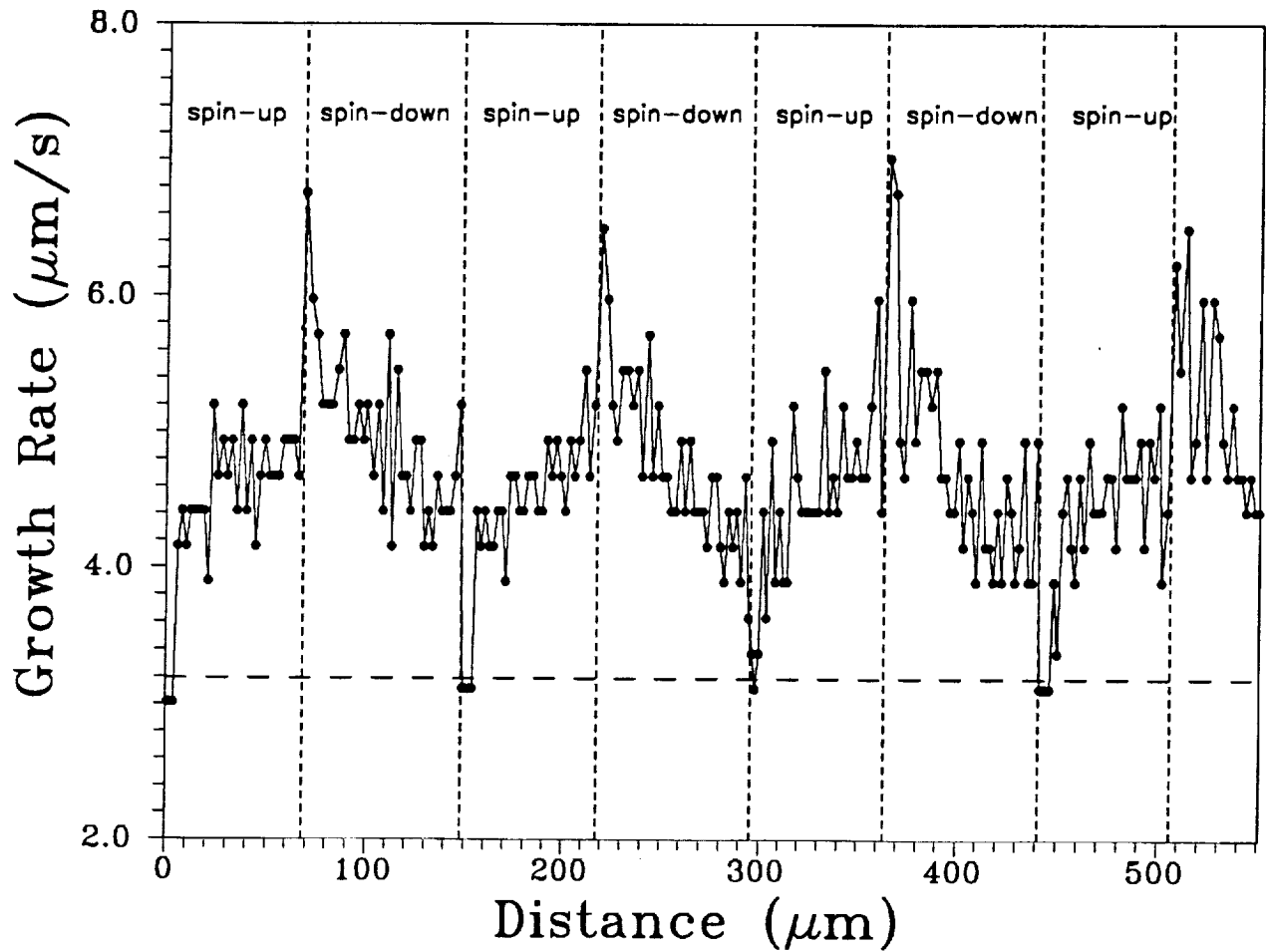
Figure 7. Growth rate over several ACRT cycles. The horizontal
dashed line represents the ampoule translation rate of
3.19 μm/s.

P. 16

Solidification of InSb-GaSb alloy and InSb

with Vibration

Weijun Yuan

Abstract Summary

The objective of this project is to determine the influence of vibration on the composition homogeneity and microstructure of alloy semiconductors solidified with the Vertical Bridgman-Stockbarger (VBS) technique. InSb-GaSb and InSb were directionally solidified in a VBS apparatus with axial vibration of the ampoule.

$In_xGa_{1-x}Sb$ with $x = 0.2$ ingots were solidified. Energy Dispersive X-ray Spectroscopy (EDS) measurements of the In concentration showed that there were no significant radial composition variations in the ingots grown both with and without vibration. The axial composition profiles corresponded to complete mixing of the melt. The quenched interface demarcation technique was used to reveal the interface shape and to measure the variation in growth rate down the ingots. Axial vibration of the ampoule did not seem to affect the average growth rate, but did increase the interface depth during the last-to-freeze parts of the ingots. Vibration appeared to decrease the number of curved boundaries, and to increase the number of straight boundaries.

InSb also was solidified in a VBS furnace with vibration. Again the number of grain boundaries was decreased by the application of vibration and the number of twins was increased, especially at the first-to-freeze part of the ingots. The Current Induced Demarcation (CID) technique was used to reveal the interface during the solidification of InSb. Because of the increased number of twins in the resulting ingots, striations caused by CID were hard to see. The details of the microstructure of InSb ingots is under investigation.

Introduction

Since GaSb and InSb are totally miscible in both liquid and solid phases, the physical properties of InSb-GaSb alloys vary continuously with composition. The InSb-GaSb system is a convenient model for all semiconductor alloy systems because of its low melting temperature and low volatility.

Due to the compositional inhomogeneity and polycrystallinity associated with bulk alloy growth, directionally solidified $In_xGa_{1-x}Sb$ generally has not been suitable for device fabrication. Many efforts have been made to understand and improve the microstructure and composition uniformity resulting from bulk crystal growth by using various techniques and growth conditions [1-5]. Because of the unavoidable thermal and composition gradients, buoyancy-induced convection is always present in the melt during solidification on Earth. It is believed that buoyancy-induced convection can result in the formation of defects in crystal grown from the melt. Therefore, there is interest in growing crystal in space and in using forced convection to eliminate the effects of free convection.

The application of forced convection to the growth of InSb-GaSb reduced the number of twins and increased its grain size [4-6]. A magnetic field was applied to the melt growth of InSb-GaSb by Sen [4]. (A magnetic field reduces natural convection and thereby may eliminate temperature fluctuations in the melt.) Use of a transverse magnetic field decreased the number of grain boundaries [4]. ACRT was used to solidify InSb-GaSb alloy in the thermally stable VBS configuration by Gray [5]. His axial composition profiles correspond to complete mixing and there were no radial composition variations with or without ACRT. The number of grain boundaries and twins in the $In_{0.2}Ga_{0.8}Sb$ ingots decreased when ACRT was applied during growth.

Application of vibration to crystal growth is another approach to enhance convection in the melt during directional solidification. Vibration has been used in melt crystal growth by many researchers [3,6-9] with a wide range of frequencies and amplitudes. For example, ultrasonic vibration at 10 KHz and vibration at the low frequency of 60 Hz and amplitudes up to 1.5 mm were used in the Czochralski growth of Te-doped InSb [6,7]. Vibration at 10-100 Hz and 0.05-1.5 mm increased the grain size and the number of twins in CdTe grown by VBS [3] and $In_xGa_{1-x}Sb$ grown by zone melting [8]. The temperature field in the melt was also affected by the application of ultrasonic vibration during the growth of $In_xGa_{1-x}Sb$ [10]. However, the mechanism by which vibration affects crystal growth from the melt is unclear.

Experiment and results

Figure 1 shows the experimental setup. The growth furnace consists of a 30 cm long hot zone and a 15 cm long cold zone separated by a 6 cm long insulated zone. A Bruel Kjaer vibrator, connected to a power amplifier and a HP function generator, allowed the ampoule to be vibrated axially at a frequency of 1 to 100 Hz at an amplitude up to 1.5 mm.

The growth material was prepared by weighing the proper amount of 6N purity of In, Ga and Sb to give the exact starting composition of $In_xGa_{1-x}Sb$ with $x=0.2$ or In and Sb for InSb. Materials were prealloyed before solidified. Table 1 shown the conditions for the growth experiments. The temperature profile of the furnace was measured using a K-type thermalcouple in an empty ampoule. Figure 2 shows the temperature profile used for $In_xGa_{1-x}Sb$. The grown ingots were 5 to 8 cm long and 0.9 cm in diameter. After finishing a run, the temperature in the furnace was lowered to that of the cold zone, then lowered to room temperature at 20°C/hr. Table 2 lists the $In_{0.2}Ga_{0.8}Sb$ ingots grown with vibration.

The quenched interface demarcation technique was used to reveal the interface shape in directional solidification of InSb-GaSb. Figure 3 shown the schedule for demarcation. First, the heater temperature was lowered quickly from 800°C to 750°C and maintained at 750°C for 5 minutes. Then the ampoule was rapidly moved down 1 mm in the furnace, followed by raising the heater temperature to 800°C. The combination of temperature lowering and the rapid movement of the ampoule resulted in fast freezing and hence caused a compositional striation in the resulting ingot.

After removing it from the growth ampoule, a grown ingot was sectioned longitudinally and cut into 2 or 3 pieces. The samples were mounted in a resin mold and mechanically polished with 320 and 600 mesh SiC disk paper and then with 5, 0.3 and 0.05 μm alumina polishing powder, respectively. The average growth rate was calculated from the distance between striations. The interface depth was measured as defined by Figure 4.

EDS was used to measure the composition of the polished samples. The electron beam voltage was 15 KeV. The spectra data were collected for 60 seconds over an area of about 2 μm^2 using a Tracor Northern Model TN-2000 attached to an ISI scanning electron microscope. The energy range was from 0 to 10 KeV with an internal potential of 10 eV. A least-squares analysis was used to get the concentration of InSb from the spectra of pure InSb, pure GaSb and InSb-GaSb samples. Both axial and radial composition profile were measured.

In order to reveal the microstructure, the mechanically polished samples were chemically etched. For InSb-GaSb samples, a solution of HNO_3+HF+H_2O (1:1:1) was used for 10 seconds at room temperature. For InSb, the sample was first etched in $NHO_3/HF/AcH/Br_2$ (100:75:60:2) for 10 seconds, then $HNO_3/0.5M$ $KMnO_4/AcH$ (1:1:1) for 6 to 10 minutes. The microstructure of the samples was examined by optical microscopy.

Vibration of the ampoule did not noticably affect the composition profile in the resulting ingots for the growth of $In_{0.2}Ga_{0.8}Sb$. Figure 5 and Figure 6 shown axial and radial composition profiles for some $In_{0.2}Ga_{0.8}Sb$ ingots. The axial compositional profiles all corresponded to complete mixing of the melt. No composition variation in the radial direction was observed for ingots grown with vibration or not. For the solidification of InSb-GaSb alloys, in order to overcome the constitutional supercooling, a high temperature gradient and a low growth rate had to be used. However, it has been shown that a high temperature gradient for the solidification of InSb-GaSb could produce a fine grain structure in the resulting ingots [2]. In our experiments, a low growth rate was used. Because of the very low freezing rate, the buildup of solute ahead of the solid/melt interface might have been avoided by diffusion alone.

With the application of axial vibration of the ampoule in the VBS growth of $In_xGa_{1-x}Sb$, the number of twins was increased and the number of grain boundaries was decreased, especially in the first half of the ingot. Figure 7 shown the microstructure of $In_{0.2}Ga_{0.8}Sb$ ingots grown with and without vibration.

Figure 8 shows the variation in growth rate for $In_{0.2}Ga_{0.8}Sb$ ingots grown with and without vibration. In the first half of the ingots, the freezing rate was greater than the ampoule lowering rate. As the growth proceeded, the freezing rate decreased and was lower than the ampoule lowering rate. Near the ends of the ingots, the growth rate increased a little for ingots grown both with and without vibration. The growth rate for $In_xGa_{1-x}Sb$ seems not to be affected by axial vibration of the ampoule. Figure 9 shows the interface shape for InSb-GaSb ingots grown with vibration. Figure 10 shows how the interface changes with the fraction solidified. In the first half of an ingot, the interface seems not to have been affected by the vibration, but in the second half, vibration increased the depth of the interface. When the frequency was increased and the amplitude was decreased, the interface depth of ingots grown with vibration became close to those grown without vibration.

In order to understand the effect of vibration on solidification using VBS techniques, some InSb ingots were solidified in a VBS furnace with vibration and CID or with periodically stopping the vibration. Figure 11 is the ampoule used for this experiment. With vibration, the number of grain boundaries decreased, but the

number of twins increased. Because many twins existed in the resulting ingots, the striations caused by turning on or off the vibration or the passage of a current pulse were difficult to see. The microstructure for these InSb ingots is under examination.

Plans

1.   Directionally solidify InSb with vibration to determine the details of the effect of vibration on the microstructure and interface.

2.   Measure the temperature change near the interface caused by vibration.

3.   Use a transparent liquid to reveal the flow pattern induced by vibration in a vertical Bridgman configuration.

References

[1]   P. Capper, J.J.G. Gosney and C.L. Jones, J. Crystal Growth 70, 356 (1984).

[2]   W. G. Coates, P. Capper, et al., J Crystal Growth 94, 959 (1989).

[3]   R.S. Feigelson and A. Bershchesky, USP 4465545.

[4]   S. Sen, PhD Thesis, University of Southern California, 1976.

[5]   R.T. Gray, PhD Thesis, Clarkson University, 1991.

[6]   H.E. Bates and M. Weinstein, J. Electrochem. Soc. Solid State Sci. 114(3), 259 (1967).

[7]   H.H. Woodburg and R.S. Lewandoskin, J. Crystal Growth 10, 6 (1971).

[8]   M. Banan, PhD thesis, Clarkson University, 1991.

[9]   T. Tsursta et al., Jap. J. Appl. Phys. 27 (1988), Suppl. 27-1, p 47.

[10] T. Tsursta, et al., Jap. J. Appl. Phys. 31 (1991), Suppl. 31-

1, p 23 .

Table 1 Experimental conditions for the growth of $In^xGa^{1-x}Sb$ and InSb

	$In_xGa_{1-x}Sb$	InSb
Hot zone temperature °C	800	600
Cold zone temperature °C	480	450
Initial InSb molar fraction	0.2	
Ampoule lowering rate mm/hr.		8

Table 2 $In_{0.2}Ga_{0.8}Sb$ ingots grown with vibration

Ingot No.	Frequency (Hz)	Amplitude(mm)
GA1	no vibration	
GV1	20	0.5
GV4	20	0.1
GV5	40	0.1
GV6	60	0.05

Note: Ampoule lowering rate: 8 mm/day

Power Amplifer

HP Function Generator

Translation Unit

B&K Vibrator

Ampoule Houlder

Ampoule and Charge

Furance

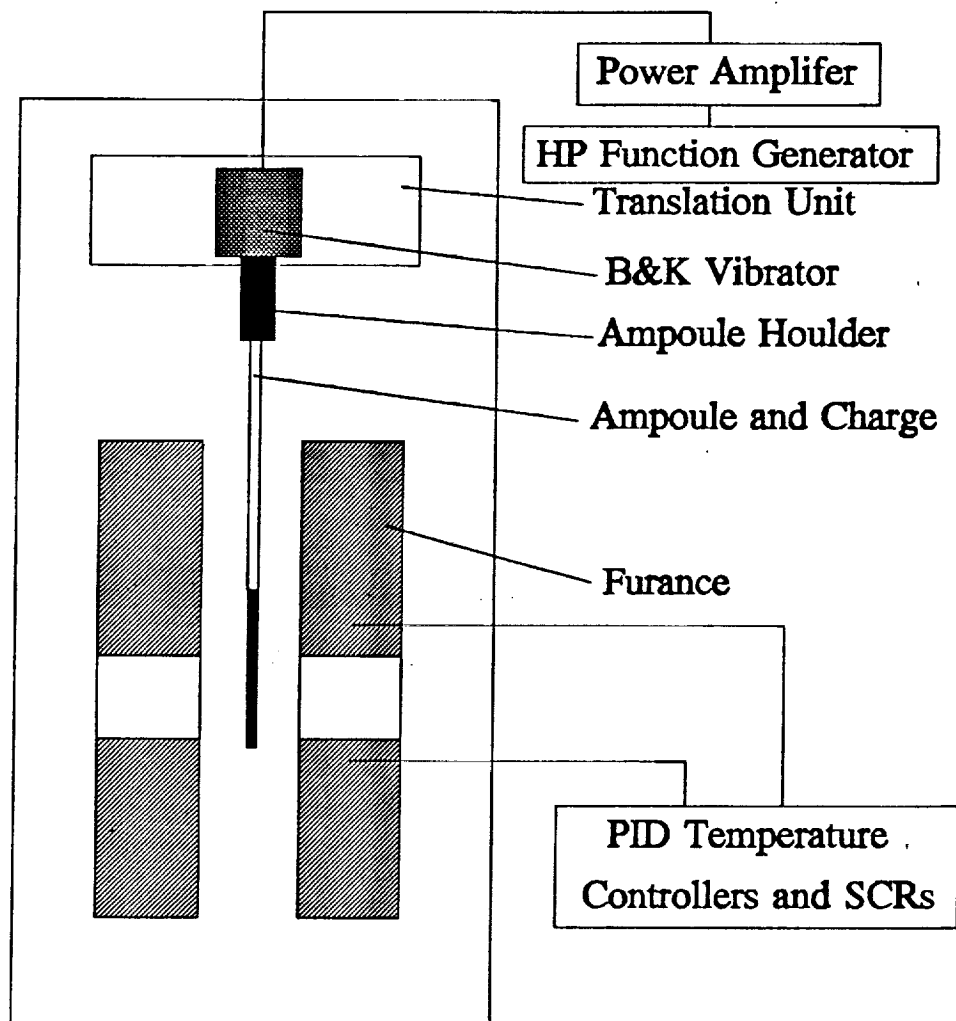PID Temperature
Controllers and SCRs

Figure 1. Experiment Setup.

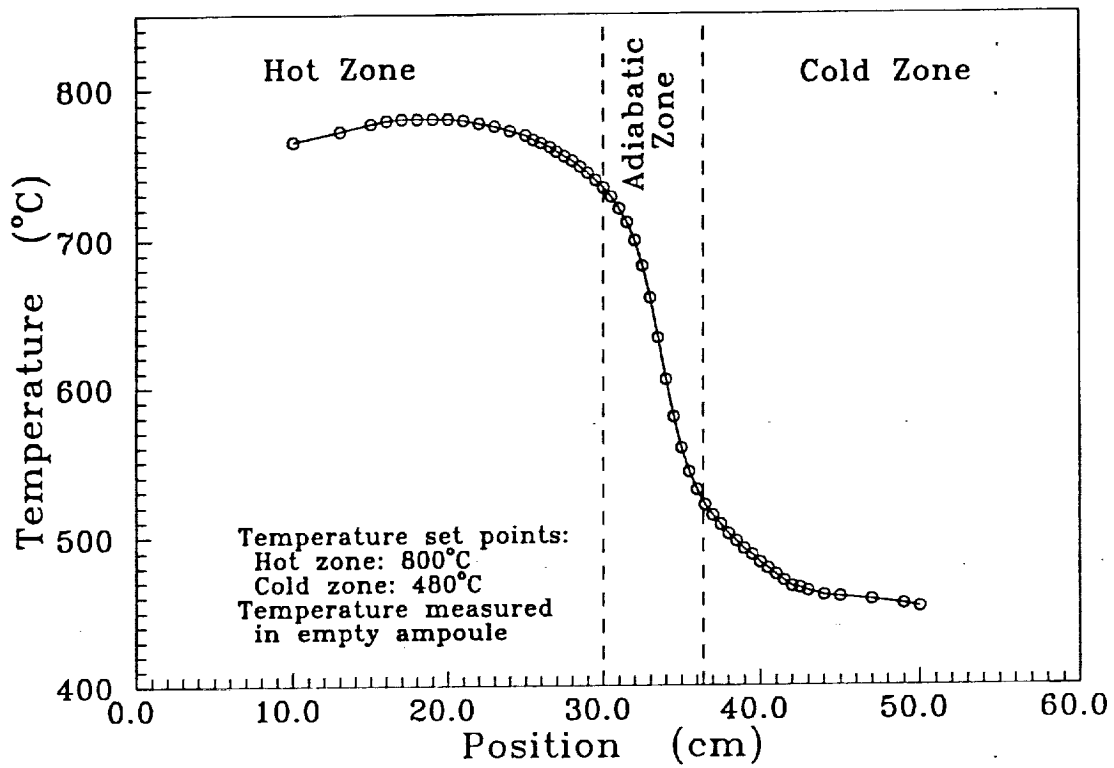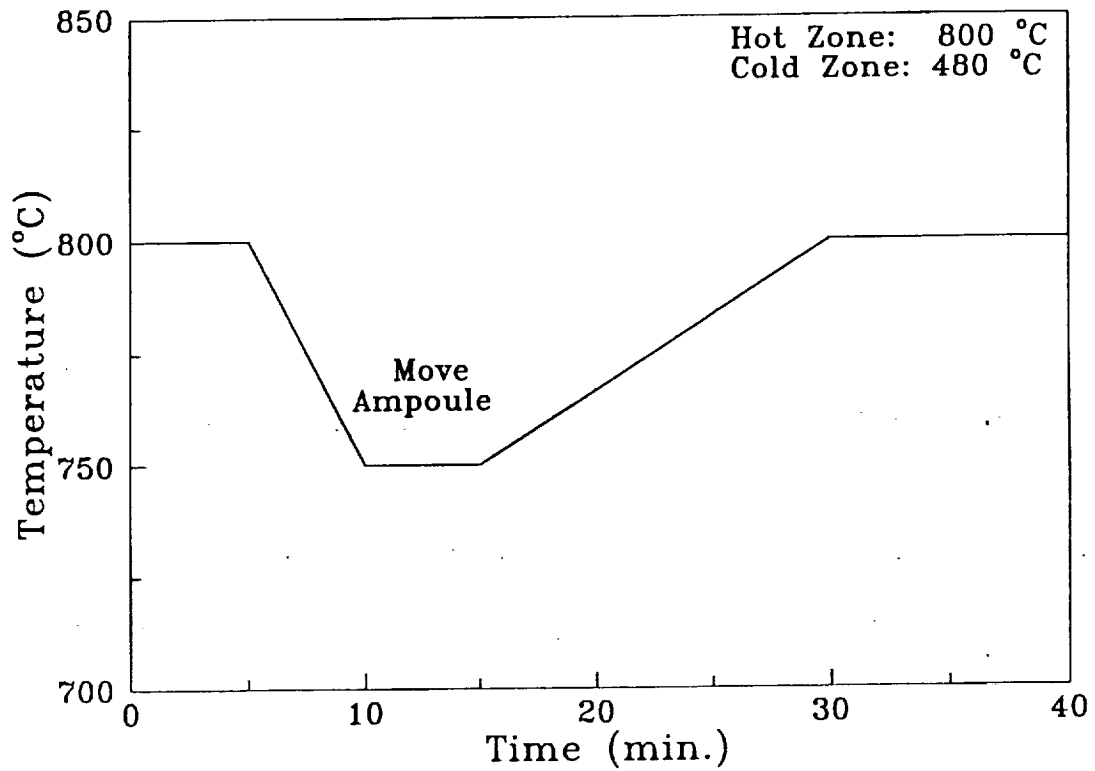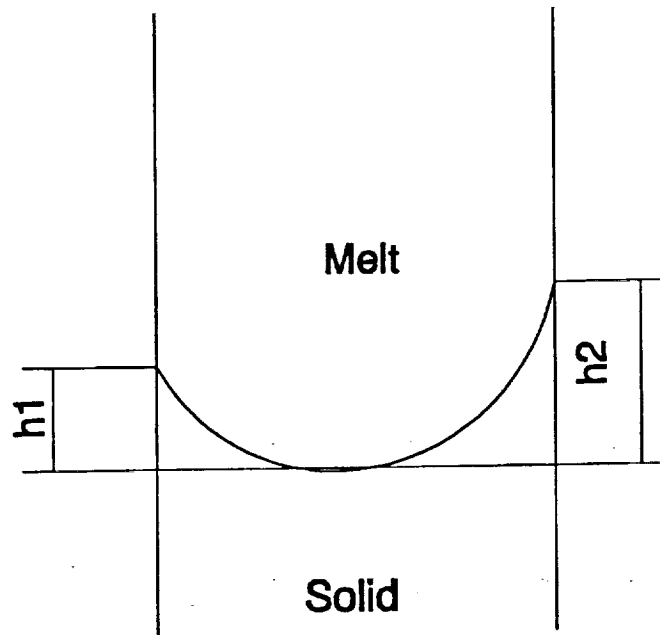**Figure 2. Temperature profile for growth of InSb-GaSb.**

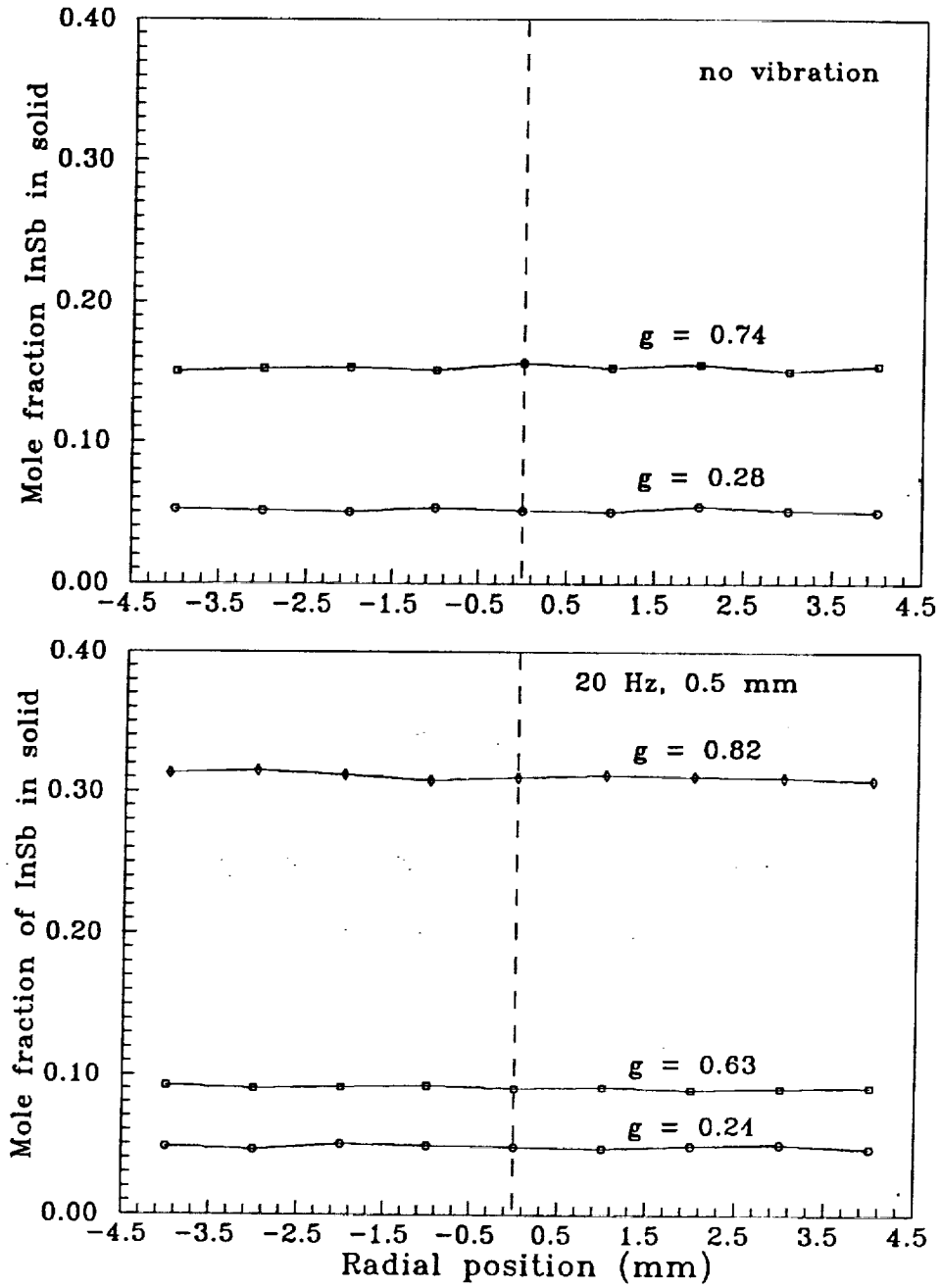**Figure 3.** Quenched interface demarcation schedule.

Figure 4. Interface depth definition.

Figure 5. Radial composition profile for $In_{0.2}Ga_{0.8}Sb$.
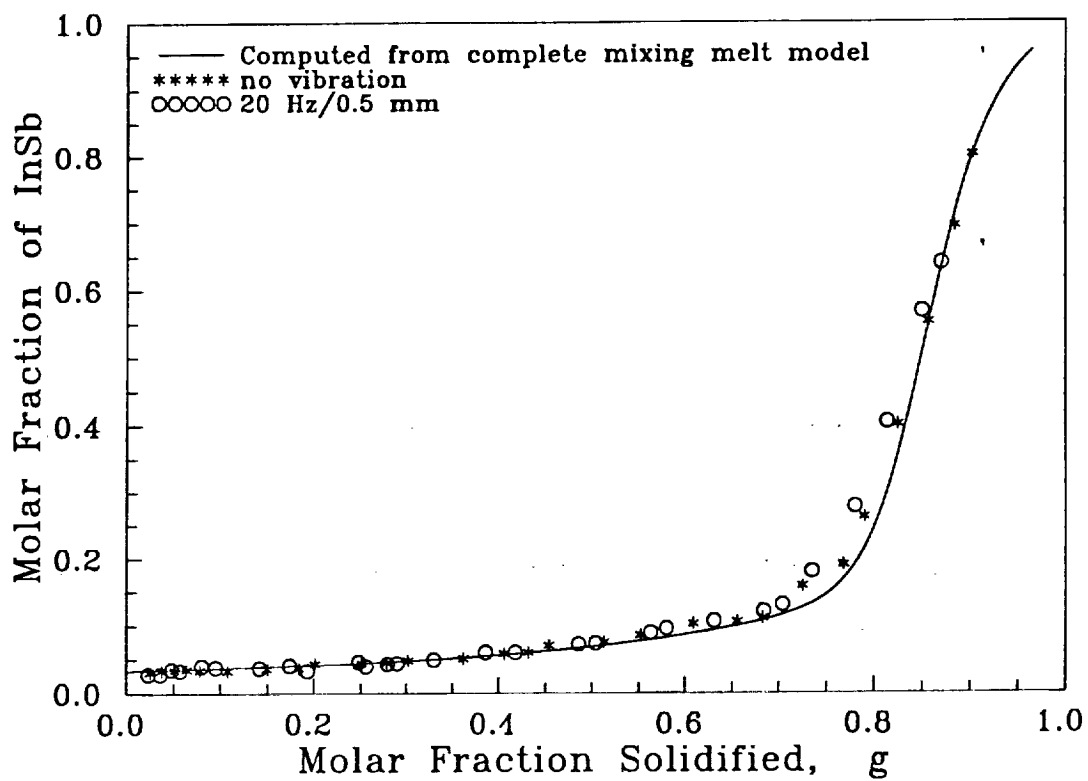
Figure 6. Axial composition profile for $In_{0.2}Ga_{0.8}Sb$.

→
growth direction
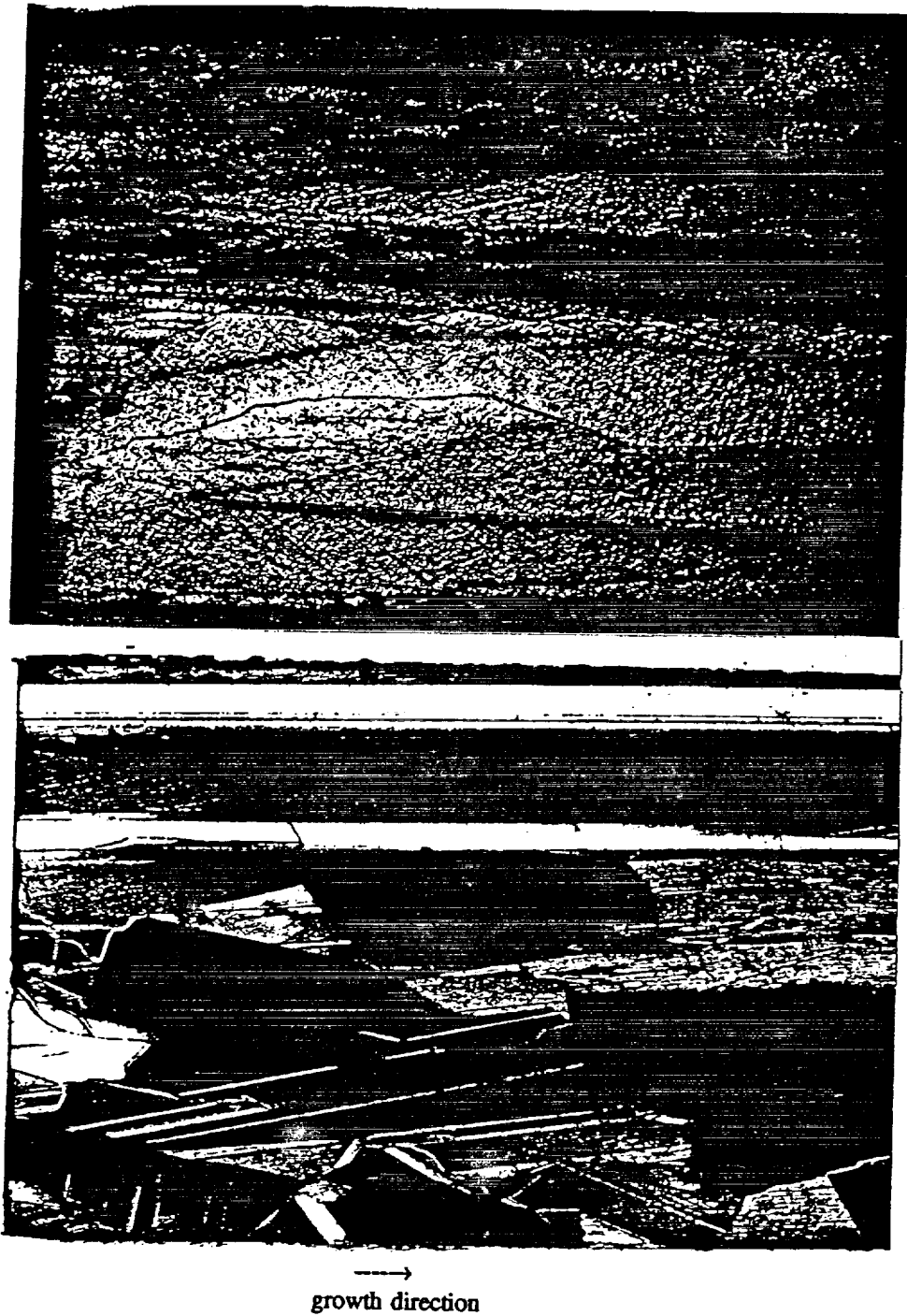
Figure 7. Microstructure for $In_{0.2}Ga_{0.8}Sb$.

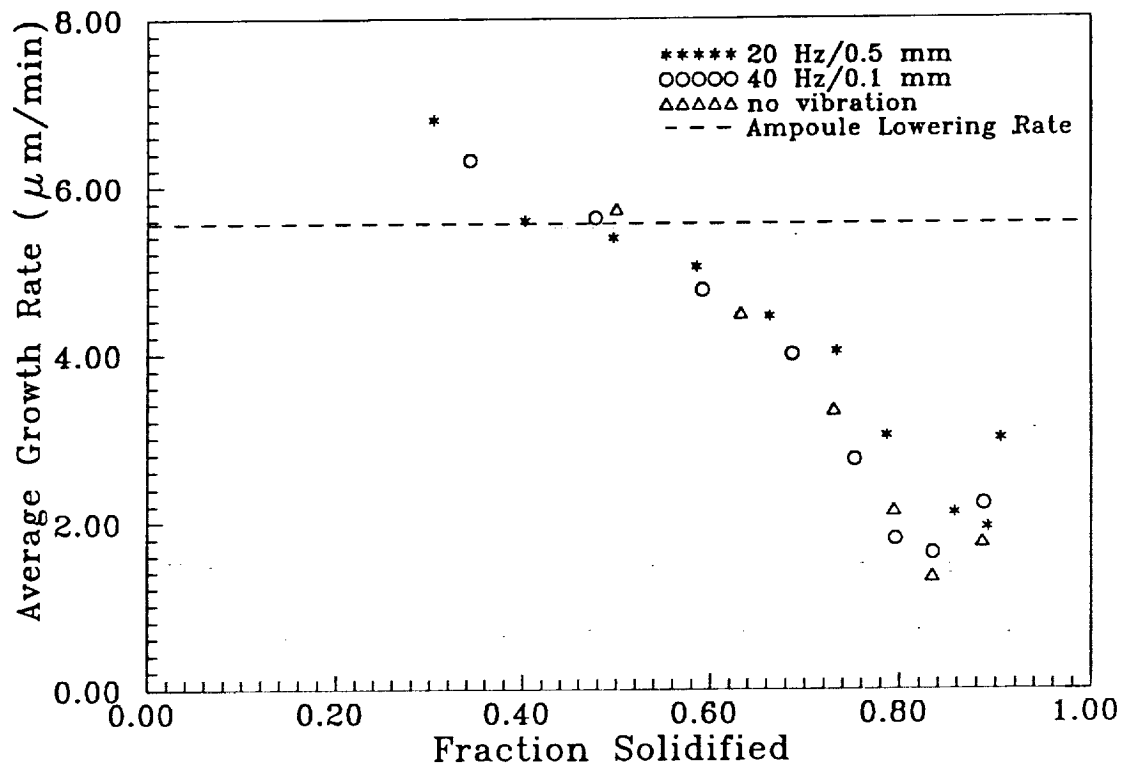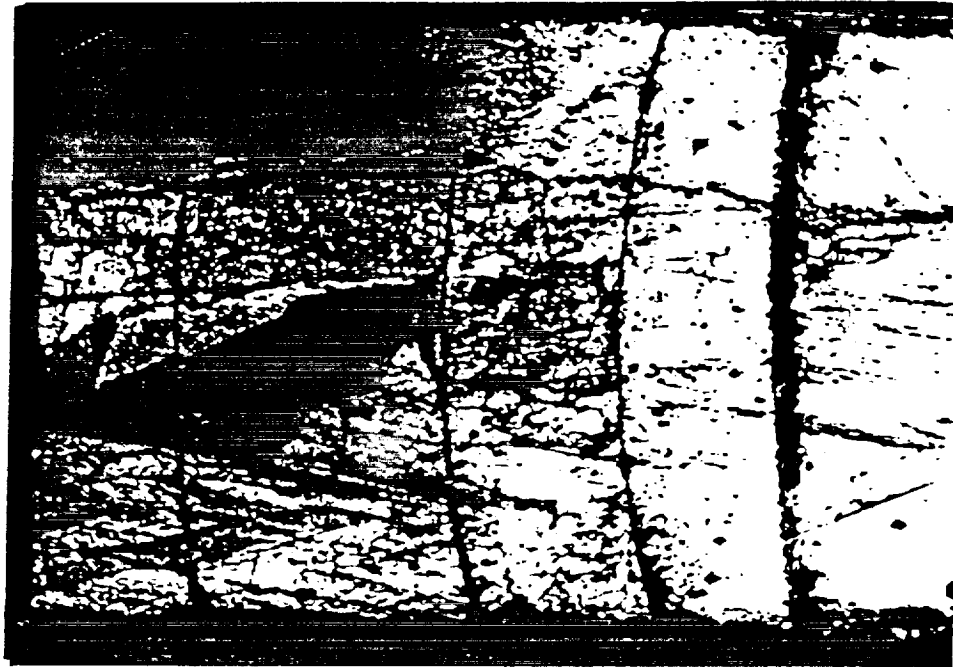Figure 8. Freezing rate for $In_{0.2}Ga_{0.8}Sb$.

growth direction

Figure 9. Interface shape for $In_{0.2}Ga_{0.8}Sb$.
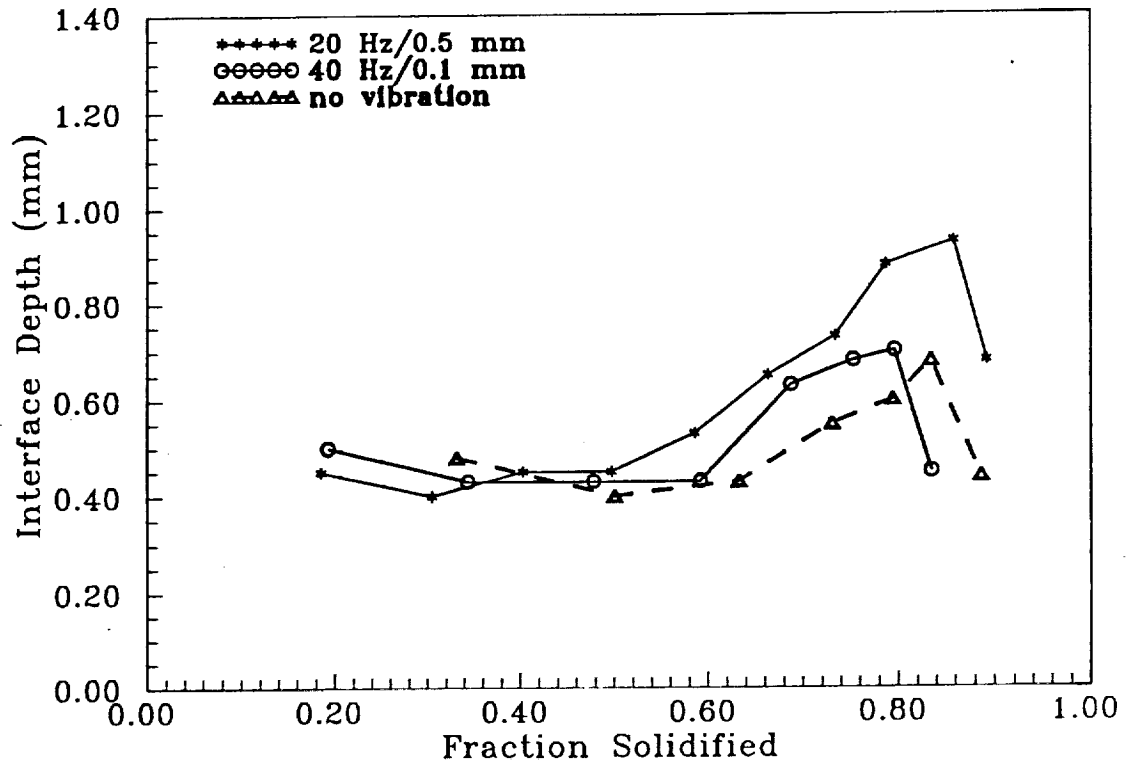
Figure 10.   Interface depth variation for $In_{0.2}Ga_{0.8}Sb$.

92A 24846

omit

Appendix A

Directional solidification of Pb–Sn eutectic with vibration

Rubens Caram [1], Mohsen Banan [2] and William R. Wilcox

Center for Crystal Growth in Space, Clarkson University, Potsdam, New York 13699-5700, USA

Pb–Sn eutectic alloy was directionally solidified at 1.4 to 3.2 cm/h with forced convection induced by axial vibration of the growth ampoule with a frequency of 10 to 40 Hz and an amplitude of 0.5 to 1.0 mm. To determine the exact growth rate, an interface demarcation technique was applied. The lamellar spacing was increased 10% to 40% in ingots solidified with vibration compared to those solidified without vibration. The number of grain boundaries was increased by vibration. The average intensity of convection in the melt under axial vibration of the ampoule was estimated by comparing the experimental results with a theoretical model.

1. Introduction

In recent years, many theoretical and experimental investigations have been performed on the effect of convection on eutectic microstructure. The main motivation for these investigations was that directional solidification of eutectic alloys can produce high quality composites with interesting anisotropic properties.

A theory for diffusion-controlled eutectic growth was presented by Jackson and Hunt [1]. Assuming a linear velocity gradient in the flow of melt across the interface, Quenisset and Naslain [2], followed later by Baskaran and Wilcox [3] and Chandrasekhar et al. [4] calculated numerically the interfacial composition during lamellar growth. The variation of composition at the solid/liquid interface was converted to changes of the undercooling at the interface. Using the extremum criterion, a relationship was derived between lamellar spacing and convection. Employing the same strategy with two different directions of flow relative to microstructure, Caram

et al. [5] determined the influence of convection on rod growth. These theoretical investigations led to the conclusion that convection increases the lamellar and rod spacing during eutectic solidification.

Eisa and Wilcox [6] and Chandrasekhar [7] experimentally studied solidification of the MnBi–Bi eutectic with the accelerated crucible rotation technique (ACRT). The MnBi rod spacing was increased by using ACRT.

Popov and Wilcox [8] directionally solidified the Pb–Sn eutectic at 1.0 and 4.6 cm/h with ACRT using a vertical Bridgman–Stockbarger technique. Application of ACRT did not change the lamellar spacing, although this did influence the rate of rotation of the spiral structures observed by Mourer and Verhoeven [9].

Another approach to enhance convection in the melt during directional solidification is application of vibration. Vibrational mixing has been utilized in melt growth by many researchers [10–19], with a wide range of amplitudes and frequencies of vibration. For example, ultrasonic vibration at 10 kHz with micron range amplitudes was used in the Czochralski growth of Te-doped InSb [10–12] and $In_xGa_{1-x}Sb$ [13]. The grain size of the Bi_2Te_3–Bi_2Se_3 eutectic system was reduced by ultrasonic agitation of the melt during direc-

---

[1] Current address: State University of Campinas, Campinas, SP, Brazil.
[2] Current address: MEMC Electronic Materials, 501 Perl Dr., St. Peters, Missouri 63376, USA.

tional solidification [14]. Vibration at frequencies of 10–100 Hz and an amplitude of 0.05 to 5 cm resulted in better grain selection in GaAs [15], CdTe [16–18], and $In_xGa_{1-x}Sb$ [19] crystals directionally solidified by zone melting and Bridgman techniques. Even though the vibration enhanced grain selection, the number of twin boundaries in CdTe [16–18] and $In_{0.2}Ga_{0.8}Sb$ [19] increased. The mechanism for modification of microstructure is not yet known.

The main objective of this work was to investigate the influence of axial vibration of the growth ampoule on the lamellar growth of Pb–Sn eutectic using a vertical Bridgman–Stockbarger technique.

2. Experimental methods

The experimental set-up consisted of a vertical Bridgman–Stockbarger crystal growth apparatus with provision for axial vibration of the growth ampoule, as shown in fig. 1. The hot and cold zones were made of Kanthal heating elements embedded in Fibrothal insulation, separated by 5 cm of zirconia insulation as an adiabatic zone. The ampoule was translated from the hot zone to the cold zone to promote solidification.

The vibration unit consisted of a Bruel Kjaer vibrator connected to a power amplifier and HP function generator. With this arrangement the ampoule could be oscillated in the axial direction, parallel to gravity, at a frequency of 0.1 to 100 Hz and an amplitude up to 1.5 mm. The acceleration due to vibration was measured using an accelerometer connected to a power amplifier and data acquisition system. Fig. 2 shows a dynamic acceleration measurement during axial vibration of the ampoule at a frequency of 20 Hz and 0.5 mm amplitude. An acceleration of $\pm 0.1g$ to $\pm 0.15g$ ($g = 9.81$ m/s^2) was measured for the range of frequencies and amplitudes utilized for our experiments.

The growth material was prepared by weighing a proper amount of 99.9999% purity Pb and Sn shots, corresponding to 61.1 wt% Pb and 38.9
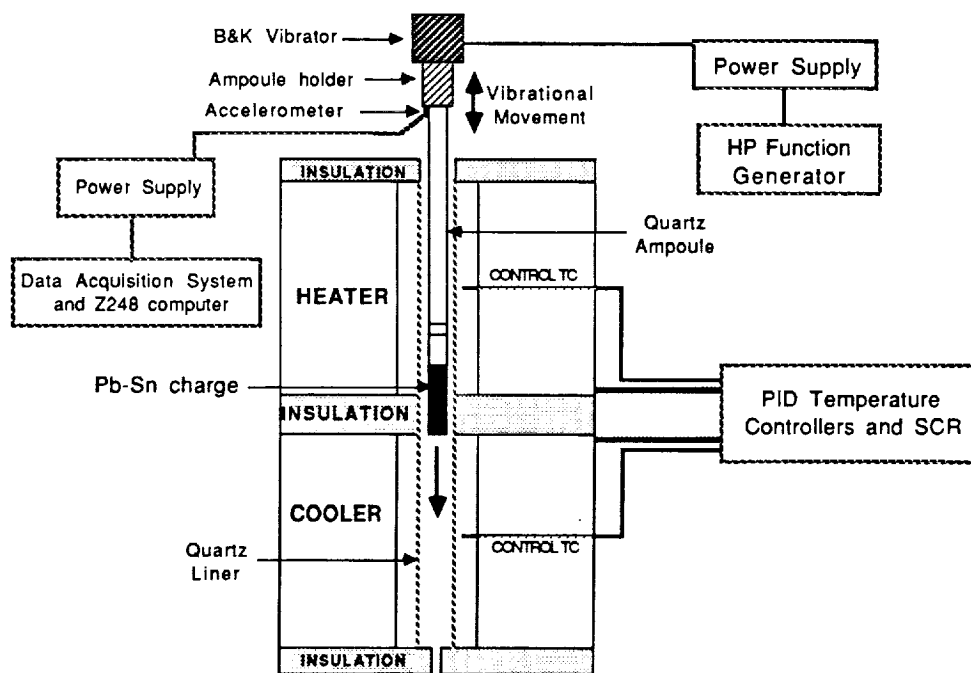

Fig. 1. Schematic diagram of the experimental set-up, including vertical Bridgman–Stockbarger furnace and a provision for axial vibration of the growth ampoule.
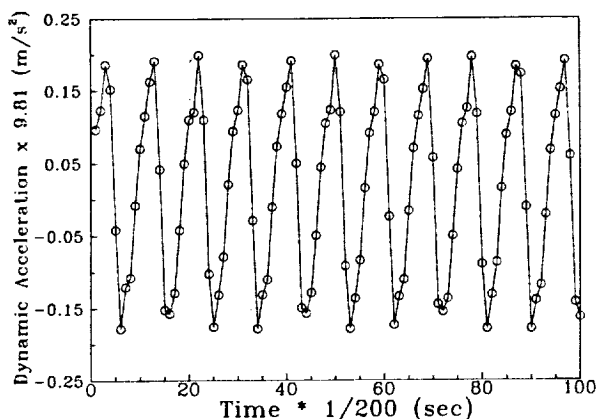
Fig. 2. Dynamic acceleration measured using an accelerometer during axial vibration of the ampoule at a frequency of 20 Hz and 0.5 mm amplitude.

3. Results and discussion

To measure the lamellar spacing, cross-sectional samples were utilized. Since the eutectic growth develops with several grains at different orientations, the use of longitudinal samples would lead to a mismeasurement of the smaller spacing. Fig. 3 presents a longitudinal slice. The lamellar spacing appears to be different in each grain because of the different orientations relative to the surface. The location of a change in the direction of lamella was taken as a grain boundary.

An intriguing result was obtained from the preliminary experiments performed without axial vibration. In these experiments, the solidification was carried out by moving the ampoule at a constant rate of 1.0 cm/h. The lamellar spacing, λ, was different from values obtained by others at the same velocity [20–23]. It was suspected that the difference between the values of lamellar spacing was due to a deviation of the growth rate from the ampoule lowering rate. Sukanek [24] showed that the freezing rate may deviate significantly from the lowering rate for directional solidification in a Bridgman–Stockbarger furnace, especially near the ends and with a large insulation zone (as used here). In our experiments, the sample was not very long (ampoule length/ampoule diameter = 12 to 15) and the insulation thickness was high (insulation zone/ampoule diameter ≈ 8). Therefore, we concluded that the deviation of the freezing rate from the translation rate might have been considerable.

To assess the deviation of the growth rate from the ampoule lowering rate, a technique was used to demarcate the liquid/solid interface periodically during the growth period. The growth ampoule was abruptly lowered 0.15 cm every one hour. This rapid movement disrupted the structure and enabled the interface shape and position to be seen in longitudinal slices. The average macroscopic freezing rate was determined by measuring the distance between these interface demarcations and knowing the frequency of suddenly lowering the ampoule. Fig. 4 shows the growth rate versus length fraction solidified in ingots 7.0 to 10 cm long. The freezing rate was

wt% Sn. Quartz ampoules containing these shots were purged with argon and sealed under a vacuum of 10^{-6} Torr. The materials were alloyed in a rocking furnace at 500°C for 6 h. Then the ampoule was transferred to the vertical Bridgman–Stockbarger furnace for directional solidification experiments. Ingots 7 to 12 cm long and 0.6 cm in diameter were directionally solidified at an ampoule lowering rate of 1.0 cm/h rate and an axial temperature gradient 40°C/cm (measured using a K-type thermocouple in an empty ampoule). The heater and cooler settings were 300 and 25°C, respectively.

Cross-sectional samples were taken from several locations along the ingot. The samples were cast in a resin mold and mechanically polished. The samples were electrochemically polished in a solution of 800 ml of absolute ethanol, 140 ml of distilled water and 60 ml of percloric acid for 60 s at room temperature. In order to reveal the microstructure, the samples were chemically etched in a solution of 1 part of glycerol, 1 part of acetic acid and 4 parts of nitric acid for 30 s at room temperature. Using such a procedure, the grain boundaries and the lamellar structure were revealed. The lamellar structure of cross-sectional and longitudinal samples was examined using optical add scanning electron microscopy.

Fig. 3. Lamellar eutectic microstructure. Growth without vibration at 1.8 cm/h: (a) longitudinal view; (b) radial view. The lamellar spacing in the radial sample was 2.5 μm. Magnification 750×.

higher at the first to freeze section of thè ingots, decreased halfway through the growth, and increased at the end of solidification. These result are in qualitative agreement with Sukanek's prediction [24].

Since the growth velocity varied, the lamellar spacing should have also varied along the ingots. Fig. 5 shows the variation of the lamellar spacing

versus the fraction solidified. For all vibration conditions, the lamellar spacing was smaller near the ends and increased in the center of the ingot, as shown in fig. 5. For the growth with vibration, the lamellar spacing was larger than without vibration.

Depending on the intensity of vibration, the use of axial vibration during direction²! solidifica-

Fig. 4. Growth rate versus length fraction solidified. The growth rate was obtained by the interface demarcation technique.

Fig. 6. Lamellar eutectic spacing obtained during this work, for several vibration conditions, compared to results obtained by Hunt and Chilton [22], Chadwick [23] and Chilton and Winegard (in ref. [23]). The growth rate was obtained by the interface demarcation technique.

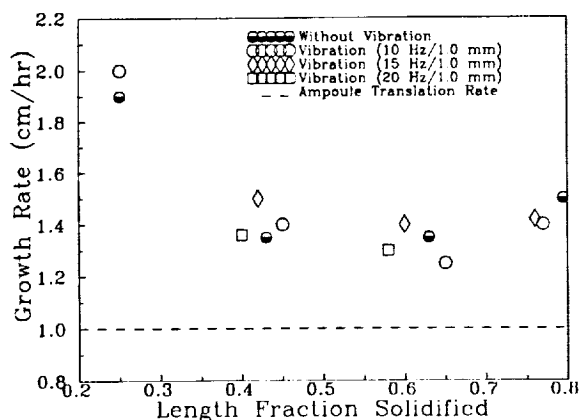tion is anticipated to enhance convection in the melt. The increased convection would be expected to cause a change in the lamellar spacing. The analysis of solidified samples in this work combined with the lamellar spacing obtained by solidification without any forced convection was in perfect agreement with the experiments conducted by Davies [20], Mollard and Flemings [21] and Chadwick [23], as well as with the equation suggested by Hunt and Chilton [22]. Fig. 6 shows a comparison of our results with and without vibration applied during solidification. The freezing rate is the actual growth rate obtained from the interface demarcation technique. This figure
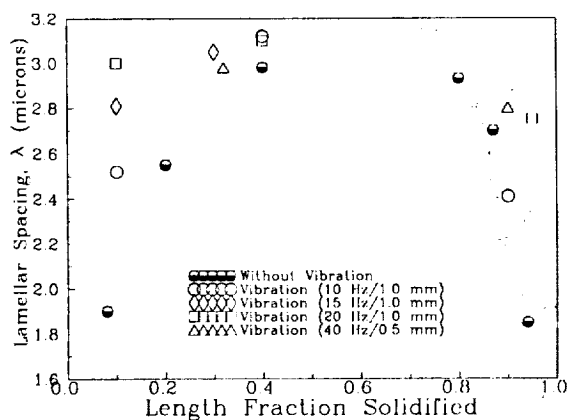
shows that the lamellar spacing was increased 10% to 45% by vibration, as compared to the ingot solidified without vibration, depending on the freezing rate. However, comparison of the ingots solidified under different vibrational conditions (amplitudes up to 1.0 mm and frequency of 10 to 40 Hz) shows 5% changes in the lamellar spacing.

Instability of the solid/liquid interface might be expected due to the oscillatory displacement of interface position according to the frequency and amplitude of vibration [25]. In a eutectic solidification, this might influence interface stability, for example causing a transition from lamellar to rod or even the cessation of regular growth. Also, vibration might cause nucleation at the interface and increase the number of eutectic grains. Such a process could lead to ingot with a more refined microstructure.

In this work, the use of several values of amplitude and frequency did not result in rod eutectic growth or a broken eutectic. In all the cases, the microstructures remained lamellar. No separation of Pb or Sn was observed, as in the ACRT experiments [8]. However, in all the experiments with vibration, independent of its amplitude and frequency, the ingots showed an increase in the eutectic grain boundaries. That is, the average

Fig. 5. Lamellar spacing as a function of length fraction solidified.

grain size decreased compared to growth under the same conditions without agitation of the melt. The examination of samples in the center of the ingot showed an increase in the number of grain boundaries. The surface spiral structure observed by Popov and Wilcox [8] and Mourer and Verhoeven [9] was not present in any ingot solidifed in this work, either with or without vibration.

The average fluid flow across the solid/liquid interface during the experiments with vibration was estimated by using Chandrasekhar et al.'s theoretical results [4]. They calculated the change in lamellar spacing for eutectic compositions of 10%, 30%, and 50% as a function of convection intensity. Interpolating their results, the change for the eutectic composition of Pb-Sn (38.9 wt%) can be estimated. For an average increase of 10% in the lamellar spacing obtained in this work with application of vibration, the use of Chandrasekhar's results led to an intensity of convection, Γ, close to 20. This value is significantly greater than the flow due to natural convection ($\Gamma \approx 0.0065$).

4. Conclusions

The influence of axial vibration of the ampoule on lamellar growth of Pb-Sn eutectics was investigated. An interface demarcation technique was used to determine the average macroscopic freezing rate along the ingot. Up to $0.15g(g = 9.81$ m/s^2) variation in acceleration was measured during axial vibration of the ampoule. Such gravitational modulations would be expected to change the fluid flow in the melt and at the interface. Axial vibration of the ampoule has increased the lamellar spacing in Pb-Sn eutectics by 10% to 45%, depending on the freezing rate. For different vibrational conditions the lamellar spacing was changed by less than 5%. Under these applied vibrational conditions, the eutectic microstructure did not change from lamellar to rod growth or irregular growth. The microstructure in all the experiments remained regular lamellar. The number of eutectic grains was increased by vibration.

References

[1] K.A. Jackson and J.D. Hunt, Trans. AIME 236 (1966) 1129.
[2] J.M. Quenisset and R. Naslain, J. Crystal Growth 54 (1981) 465.
[3] V. Baskaran and W.R. Wilcox, J. Crystal Growth 67 (1984) 343.
[4] S. Chandrasekhar, G.F. Eisa and W.R. Wilcox, J. Crystal Growth 78 (1986) 485.
[5] R. Caram, S. Chandrasekhar and W.R. Wilcox, J. Crystal Growth 106 (1990) 294.
[6] G.F. Eisa and W.R. Wilcox, J. Crystal Growth 78 (1986) 159.
[7] S. Chandrasekhar, PhD Thesis, Clarkson University, Potsdam, NY (1987).
[8] D. Popov and W.R. Wilcox, J. Crystal Growth 78 (1986) 175.
[9] D.P. Mourer and J.D. Verhoeven, J. Crystal Growth 37 (1977) 197.
[10] M. Kumagawa, H. Oka, N.V. Quang and Y. Hayakawa, Japan. J. Appl. Phys. 21 (1980) 753.
[11] Y. Hayakawa, Y. Sone, K. Tatsumi and M. Kumagawa, Japan. J. Appl. Phys. 21 (1982) 1273.
[12] Y. Hayakawa and M. Kumagawa, Japan. J. Appl. Phys. 22 (1983) 206.
[13] T. Tsuruta, Y. Hayakawa and M. Kumagawa, Japan. J. Appl. Phys. 28, Suppl. 28-1 (1989) 36.
[14] H.E. Bates and M. Weinstein, J. Electrochem. Soc., Solid State Sci. 114 (1967) 259.
[15] C. Li, NASA Tech. Briefs (Spring 1977) 147.
[16] H.H. Woodbury and R.S. Lewandowski, J. Crystal Growth 10 (1971) 6.
[17] R.S. Feigelson and A. Bershchevsky, US Patent No. 4,465,545, August 14 (1984).
[18] W.S. Liu, M.F. Wolf, D. Elwell and R.S. Feigelson, J. Crystal Growth 82 (1987) 589.
[19] M. Banan, PhD Thesis, Clarkson University, Potsdam, NY (1991).
[20] V. de L. Davies, J. Inst. Metals 93 (1964-1965) 3639.
[21] F.R. Mollard and M.C. Flemings, Trans. TMS-AIME 239 (1967) 1534.
[22] J.D. Hunt and J.P. Chilton, J. Inst. Metals 92 (1963-1964) 21.
[23] G.A. Chadwick, J. Inst. Metals 92 (1963-1964) 18.
[24] P.C. Sukanek, J. Crystal Growth 58 (1982) 208.
[25] B.T. Murray, S.R. Coriell and G.B. McFadden, J. Crystal Growth 110 (1991) 713.

An experimental approach to determine the heat transfer coefficient in directional solidification furnaces

Mohsen Banan, Ross T. Gray and William R. Wilcox

Center for Crystal Growth in Space and School of Engineering, Clarkson University, Potsdam, New York 13699, USA

The heat transfer coefficient between a molten charge and its surroundings in a Bridgman furnace was experimentally determined using in-situ temperature measurement. The ampoule containing an isothermal melt was suddenly moved from a higher temperature zone to a lower temperature zone. The temperature–time history was used in a lumped-capacity cooling model to evaluate the heat transfer coefficient between the charge and the furnace. The experimentally determined heat transfer coefficient was of the same order of magnitude as the theoretical value estimated by standard heat transfer calculations.

1. Introduction

A variety of directional solidification techniques are used for preparation of materials, especially for growth of single crystals. These techniques include the vertical Bridgman–Stockbarger, horizontal Bridgman, zone-melting, and gradient freeze methods. It is time consuming and costly to experimentally determine the optimal thermal conditions of a furnace utilized to grow a specific material. Hence, it is desirable to employ analytical and numerical models to assist in determining the optimal thermal conditions for a specific growth system, e.g. vertical Bridgman–Stockbarger technique [1–6]. Such calculations are handicapped by limited knowledge of the growth environment's thermal characteristics.

The heat transfer coefficient, defined as the ratio of the heat flux to the temperature difference between the material and the furnace, is an important thermal parameter in a growth system. The heat transfer coefficient manifests itself in the heat transfer models as the Biot number hR/k, where h is the heat transfer coefficient, R is the sample radius, and k is the thermal conductivity of the sample. The Biot number may be regarded as the ratio of the ease of heat exchange with the furnace to heat conduction through the charge.

Chang and Wilcox [1] showed that increasing the Biot number in Bridgman growth affects the position and shape of the isotherms in the furnace. The sensitivity of interface position to the hot and cold zone temperatures is greater for small Biot number.

Fu and Wilcox [2] showed that decreasing the Biot numbers in the hot and cold zones of a vertical Bridgman–Stockbarger system results in isotherms becoming less curved. The planar isotherms lie in the lower portion of the adiabatic zone when the heater's Biot number is larger than the cooler's Biot number. Increasing the cooler's Biot number moved the position of the planar interface toward the upper section of the adiabatic zone.

Although the heat transfer coefficient may be estimated from heat transfer principles [5,7], considerable uncertainties make an experimental value preferred. We report an experimental approach to determine the average heat transfer coefficient between the growth material and the furnace. This is accomplished by in-situ temperature measurement of a transiently cooled object, i.e. melt or solid contained in an ampoule. In this technique, an isothermal charge at temperature T_0 is suddenly moved to a chamber at temperature T_∞. The temperature of the charge is measured as a function of

time with a thermocouple. The data obtained are used in a lumped-capacity model to calculate the average heat transfer coefficient between the molten charge and its surroundings. A GaSb charge was used to demonstrate the method. The validity of the lumped-capacity model was examined by use of the one-dimensional transient heat transfer problem between a rod and its surroundings and comparing the results of this analysis with the lumped-capacity solution. The one-dimensional transient problem considers radial temperature gradients in the rod.

2. Lumped-capacity model

The value of the heat transfer coefficient depends on the geometry of the system as well as the physical properties and temperatures of the material and its environment. A simple, but important method, based on a lumped-capacity solution [8] can be used to determine the average heat transfer coefficient between an object and its surroundings from the transient cooling of the object. The analysis assumes that the object is isothermal. This object at temperature T_0 is introduced suddenly into an environment at temperature T_∞. The heat transfer coefficient is calculated from the change in temperature of the object as a function of time. The analytical development of the lumped-capacity model is presented in ch. 4, pp. 101–108, of Ozisik [8]. The temperature–time relationship is given in non-dimensional form as:

$$\ln \theta = (-2 \text{ Bi}) \tau, \tag{1}$$

where $\text{Bi} = \bar{h}R/k$, $\theta = (T - T_\infty)/(T_0 - T_\infty)$, $\tau = \alpha t/R^2$, and α is the thermal diffusivity of the object. The Biot number is found from the slope of a $\ln \theta$ versus τ plot and the heat transfer coefficient is given by:

$$\bar{h} = \text{Bi } k/R. \tag{2}$$

In our experiments, the object consisted of a molten GaSb charge contained in a quartz ampoule (discussed in detail in the experimental section). The environment was a vertical Bridgman–Stockbarger furnace. The ampoule wall added a

resistance to the heat transfer between the charge and the furnace. To include the effect of such resistance on the heat transfer coefficient, some modifications of the thermophysical properties in eqs. (1) and (2) were necessary. (A similar approach was undertaken by Naumann [5].) The mass weighted effective thermal conductivity and thermal diffusivity are defined as follows:

$$k_{\text{eff}} = \frac{\rho_c V_c k_c + \rho_a V_a k_a}{\rho_c V_c + \rho_a V_a}, \tag{3}$$

$$\alpha_{\text{eff}} = \frac{k_{\text{eff}}}{\rho_{\text{avg}} c_{\text{eff}}} = \frac{(\rho_c V_c k_c + \rho_a V_a k_a)(V_c + V_a)}{(\rho_c V_c c_c + \rho_a V_a c_a)(\rho_c V_c + \rho_a V_a)}, \tag{4}$$

where all parameters are defined in the table of nomenclature. The effective heat transfer coefficient then becomes:

$$\bar{h}_{\text{eff}} = \text{Bi}_{\text{eff}} k_{\text{eff}}/R_a, \tag{5}$$

where R_a is the outer radius of the ampoule and Bi_{eff} is found from the slope of the $\ln \theta$ versus $\tau_{\text{eff}} = \alpha_{\text{eff}} t/R_a^2$ plot.

3. Validity of the lumped-capacity model

In order to determine the validity of the lumped-capacity model for different ranges of the Biot number, a similar model was solved which takes radial temperature gradients in the sample into account. This model assumes that the heat flow is axisymmetric, the temperature in the rod is uniform in the axial direction, and the density, specific heat, and thermal conductivity of the rod are independent of temperature. It is valid for all values of the Biot number. The solution to this problem is given in ch. 7, pp. 201–202, of Carslaw and Jaeger [9]. When this solution is simplified to give the dimensionless temperature at the centerline of the rod, the following equation results:

$$\theta = \frac{T - T_\infty}{T_0 - T_\infty}$$

$$= 2 \sum_{n=1}^{\infty} \frac{\text{Bi}}{J_0(\Gamma_n)(\Gamma_n^2 + \text{Bi}^2)} \exp(-\Gamma_n^2 \tau), \tag{6}$$

where the eigenvalues Γ_n are roots of the equation:

$$\Gamma_n J_1(\Gamma_n) = \text{Bi } J_0(\Gamma_n), \tag{7}$$

and J_0 and J_1 are Bessel functions of order zero and one, respectively. For the range of Biot numbers studied, ten terms of the infinite series were determined to yield an accuracy of more than 5 significant digits in θ.

When the series in eq. (6) is truncated after the first term, the following equation is obtained:

$$\ln \theta' = \ln\left\{\frac{2\text{ Bi}}{J_0(\Gamma_1)(\Gamma_1^2 + \text{Bi}^2)}\right\} - \Gamma_1^2 \tau. \tag{8}$$

In order to determine when the series could be truncated after the first term, the error in truncation had to be determined as a function of dimensionless time τ and Biot number. The relative truncation error was defined to be $(\theta' - \theta)/\theta$, where θ is the exact solution which was taken as the value of θ when the series was truncated after ten terms. The dimensionless time τ_{crit} beyond which the truncation error is less than 0.01 is plotted in fig. 1 for values of the Biot number between 0 and 0.9. For values of the Biot number between about 0.05 and 0.9, the critical dimen-
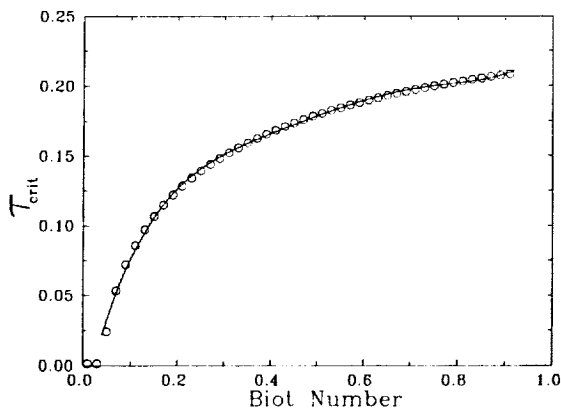

Fig. 1. The dimensionless time τ_{crit} versus Biot number past which the error in θ caused by truncation of eq. (6) after the first term is less than 0.01. The line represents the 5th order polynomial fit given by eq. (9).
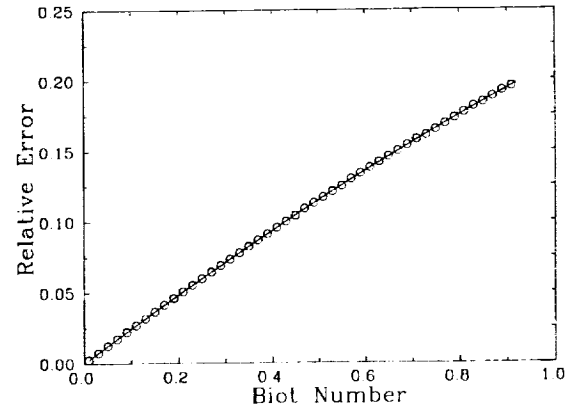
Fig. 2. Relative error caused by assuming the Biot number equals -0.5 times the slope of a $\ln \theta$ versus τ plot. The line represents the 2nd order polynomial fit given by eq. (10).

sionless time is given by the 5th order polynomial fit:

$$\tau_{crit} = 3.02 \text{ Bi}^5 - 8.54 \text{ Bi}^4 + 9.32 \text{ Bi}^3 - 5.03 \text{ Bi}^2$$
$$+ 1.48 \text{ Bi} - 0.0302. \tag{9}$$

Eq. (8) is accurate to within 1% in dimensionless temperature for dimensionless times greater than τ_{crit}. Therefore, a plot of $\ln \theta$ versus τ should be linear after time τ_{crit}. If a linear regression analysis is carried out on experimental data at dimensionless times greater than τ_{crit}, Γ_1 is given by the square root of the negative of the slope. This experimentally determined value of Γ_1 can then be used in eq. (7) to calculate the Biot number.

Eq. (8) is similar to the lumped-capacity solution, except that the intercept is not zero and the slope is $-\Gamma_1^2$ as compared to -2 Bi from the lumped-capacity model. The validity of the lumped-capacity solution can be assessed by calculating the relative error caused by assuming the Biot number equals the negative of the slope of a $\ln \theta$ versus τ plot divided by two. The relative error can be defined as $(\text{Bi} - \Gamma_1^2/2)/\text{Bi}$, where Bi is the actual Biot number and Γ_1 is calculated from eq. (7). The relative error is plotted in fig. 2 as a function of Biot number and is given by the 2nd order polynomial fit:

$$\text{relative error} = -0.0373 \text{ Bi}^2 + 0.248 \text{ Bi}, \tag{10}$$

for Biot numbers between 0 and 0.9. The relative error is almost a linear function of Biot number in this region.

This analysis suggests that care must be taken when applying the lumped-capacity model to experimental data. A linear regression analysis should only be done for values of $\tau > \tau_{crit}$. When the Biot number is large, most of the temperature change could occur before τ_{crit} and the error in assuming the slope equals -2 Bi becomes large. Also, the experimental error in temperature measurement causes large errors in the value of ln θ when T approaches T_∞. This is best demonstrated by example. Let us consider the case when $T_0 = 800\,°C$, $T_\infty = 700\,°C$, and the error in measurement of the object's temperature is $1°C$. If the temperature of the object T is $750°C$, the error in the resulting value of ln θ is only 3%. However, when the temperature of the object is $701°C$, the error is 15%. Another important point when applying the lumped-capacity model is that the straight line should not be forced through the origin. A two-parameter regression analysis should be performed, as suggested by eq. (8).

4. Experimental technique

The lumped-capacity method was demonstrated using an ampoule and thermocouple arrangement containing molten GaSb situated in the heater of a Bridgman–Stockbarger furnace at temperature T_0. The ampoule was moved suddenly to a region of different temperature T_∞. The temperature versus time data were collected as the melt equilibrated to the new temperature and the lumped-capacity model was used to determine the heat transfer coefficient between the ampoule and furnace.

The experimental apparatus consisted of a three-zone vertical Bridgman–Stockbarger furnace. The heating zones of the furnace were made of Kanthal heating elements embedded in Fibrothal insulation. The 5 cm long adiabatic zone was fabricated from zirconia insulation. Quartz tubing was used as a liner in the furnace. Two K-type thermocouples, inserted halfway into the heaters between the furnace wall and the liner,
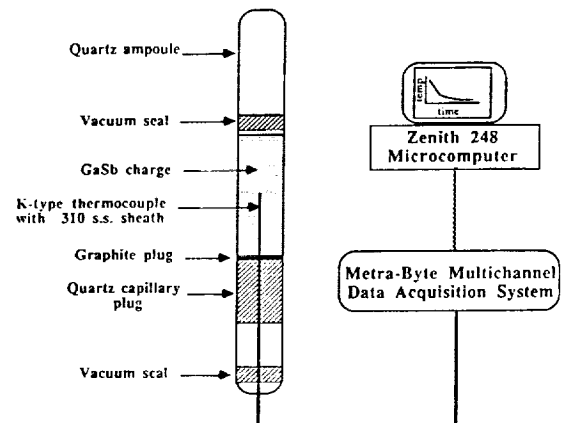
Fig. 3. Schematic diagram of ampoule and thermocouple arrangement with data acquisition system for in-situ temperature measurements.

were used for control. Both ends of the furnace were plugged to eliminate the chimney effect.

The 0.9 cm inner diameter and 1.1 cm outer diameter quartz growth ampoule, shown in fig. 3, was loaded with a 7 cm long GaSb charge, compounded from six-9s purity Ga and Sb in a rocking furnace for 5 h at 820°C. The temperature in the melt was measured using a 0.041 cm diameter grounded K-type thermocouple with a 310 stainless steel sheath and MgO as insulation (made by General Measurements). The tip of the thermocouple was positioned 3 cm into the ampoule at the center of the charge.

The molten charge was allowed to reach thermal equilibrium with the surroundings prior to each experiment. For experiments 1 and 2, the ampoule was suddenly moved from the lower zone to the upper zone and held firmly. While for experiment 3, the ampoule started in the upper zone and was moved to the lower zone. The thermocouple output was collected versus time using a data acquisition system.

5. Results

5.1. Experimental determination of heat transfer coefficients

Fig. 4 shows the actual thermocouple readings collected from the molten GaSb during experi-

Fig. 4. Thermocouple readings in molten GaSb. The circles, triangles, and squares represent the data of experiments 1, 2, and 3, respectively.

Fig. 5. Experimental data and the resulting linear fit ($R^2 = 0.9993$) for experiment 1.

ments 1, 2, and 3 (see also table 1). The logarithm of the dimensionless temperature θ was plotted versus dimensionless time τ_{eff} for each experiment. Linear regression analyses using NCSS Statistical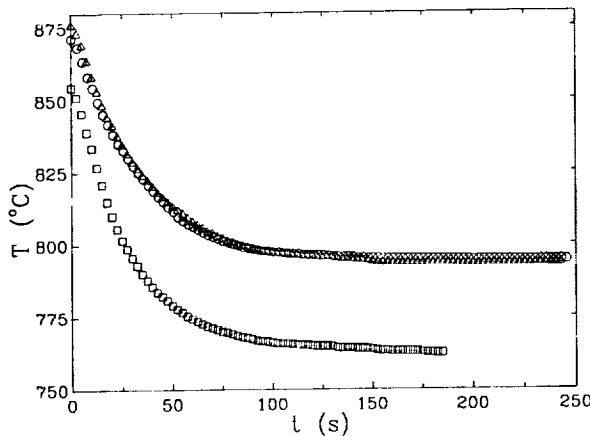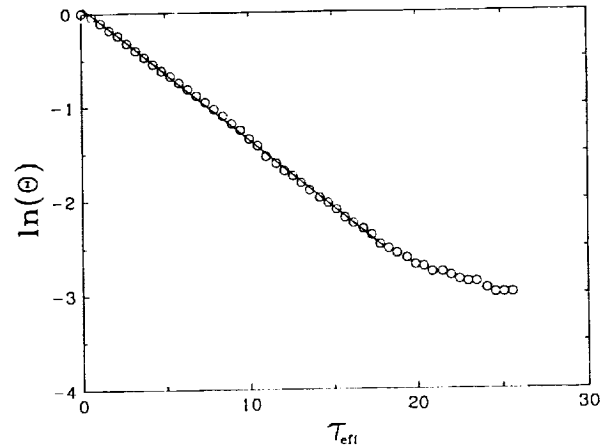 Software were performed to determine the slopes and intercepts of these plots. The plot for experiment 1 is shown in fig. 5.

The linear regression analysis for experiment 1 was performed on the data for τ_{eff} between 0.1 and 18. There are two reasons that these limits for τ_{eff} were chosen. The value of τ_{crit}, beyond which the relationship between ln θ and τ_{eff} is linear, is less than 0.1. Also, the experimental data tend to bend upward beyond $\tau_{eff} = 18$. The reason for this is the magnification of experimental error at small values of θ. (Both of these explanations are discussed fully in section 3). The resulting linear fit is $\theta = (-0.142 \pm 0.0006)\tau + (0.0697 \pm 0.0059)$. The uncertainty values are 95% confidence limits on

Table 1
Listing of the temperatures of the upper zone T_u, lower zone T_ℓ, the initial charge temperature T_0, and final steady-state charge temperature T_∞ for experiments 1, 2, and 3

Experiment	Temperature (°C)			
	T_u	T_ℓ	T_0	T_∞
1	800	890	871	792
2	800	890	876	794
3	870	780	855	762

the slope and intercept, which can be transformed into 95% confidence limits on the Biot number. The lumped-capacity solution leads to a Biot number of 0.0712 ± 0.0003 determined from the slope. The value of the Biot number determined using the model accounting for radial temperature gradients is 0.0725 ± 0.0003.

The same analysis as above was performed for experiments 2 and 3. The linear regression analysis for experiment 2 was performed on the data for τ_{eff} between 0.1 and 20. The linear fit is $\theta = (-0.138 \pm 0.0004)\tau + (0.0407 \pm 0.0042)$. The lumped-capacity solution leads to a Biot number of 0.0689 ± 0.0002. The value of the Biot number determined using the model accounting for radial temperature gradients is 0.0701 ± 0.0002. For experiment 3, the linear regression analysis was performed on the data for τ_{eff} between 0.1 and 15. The linear fit is $\theta = (-0.171 \pm 0.0008)\tau + (0.0522 \pm 0.0073)$. The lumped-capacity solution leads to a Biot number of 0.0855 ± 0.0004. The value of the Biot number determined using the model accounting for radial temperature gradients is 0.0873 ± 0.0004.

The heat transfer coefficients obtained for experiments 1, 2, and 3 are presented in table 2. There are two different values for each experiment. One is from the lumped-capacity model and one is from the model which accounts for radial temperature gradients.

Table 2
Comparison of the experimentally determined and theoretically estimated values of the heat transfer coefficient for experiments 1, 2, and 3

Experiment	h (W/cm²·K)		
	Lumped-capacity model	Radial model	Theoretical estimation
1	0.0189	0.0193	0.0220
2	0.0183	0.0186	0.0220
3	0.0227	0.0232	0.0189

5.2. Theoretical estimation of heat transfer coefficients

The heat transfer coefficient between the ampoule wall and the furnace could also be estimated by a simple heat transfer formulation. The heat transfer coefficient is derived by summing the heat transfer by radiation and conduction through the air gap between the ampoule and the furnace wall in a concentric cylindrical system and equating it to the heat flux per unit area Q through the ampoule containing the growth materials:

$$Q = \bar{h}(T_h - T_a) = \sigma \epsilon F(T_h^4 - T_a^4)$$
$$+ \frac{k_{air}(T_h - T_a)}{R_a \ln(R_f/R_a)}. \qquad (11)$$

The contribution of natural convection between the ampoule and the furnace was determined by computing the Grashof number in the air gap between the ampoule and the quartz liner. We estimated the Grashof number for our experiments to be 246 and concluded that the contribution of natural convection to the heat transfer was insignificant [10]. Therefore, the convective heat transfer term was not included in eq. (11).

The view factor $F = 0.9$ was approximated using the view factor for finite-length concentric cylinders (i.e. furnace–ampoule) [8]. The ampoule temperature T_a was assumed to be the same as the temperature of the molten charge, since the ampoule wall was only 0.1 cm thick compared to the 0.45 cm charge radius. The steady-state temperature reading in the charge T_∞ and the temper-

ature of the control thermocouple were used for T_a and T_h, respectively. The values of $T_a = 793°C$ and $T_h = 800°C$ for experiments 1 and 2, and $T_a = 762°C$ and $T_h = 780°C$ for experiment 3 were used in calculation of the heat transfer coefficients.

The values of $\bar{h}$ calculated for experiments 1, 2, and 3 were 0.0220, 0.0220, and 0.0189 W/cm²·K, respectively. The estimated heat transfer coefficients are compared with the experimentally determined values in table 2.

6. Discussion

Fig. 6 depicts the comparison between the Biot numbers calculated from the lumped-capacity model (Bi = $-m/2$) and from the model including radial temperature gradients ($\Gamma_1 = \sqrt{-m}$, Bi $= \Gamma_1 J_1(\Gamma_1)/J_0(\Gamma_1)$). The horizontal and vertical lines in the figure represent 95% confidence limits on the values of the Biot number. The three data points would fall along the solid diagonal line if the results from the lumped-capacity model agreed exactly with the theory that considers radial temperature gradients in the charge. The dashed line
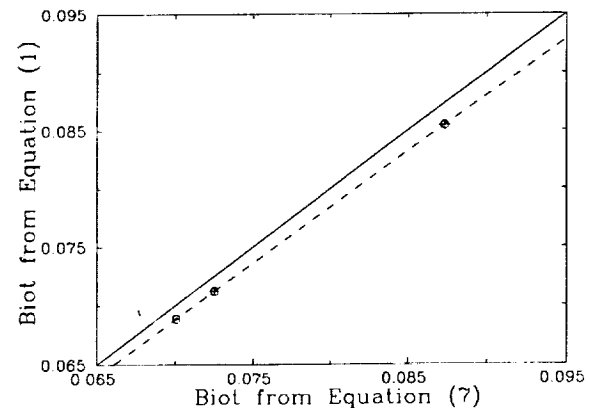
Fig. 6. Comparison between the Biot numbers calculated from the slope using eq. (1) (lumped-capacity model) and using eq. (7). The horizontal and vertical lines in the figure represent 95% confidence limits on the values of the Biot number. The dashed line represents the calculated relative error between the two models and is given by eq. (10).

represents the calculated relative error between the two models and is given by eq. (10).

The Biot numbers calculated from the model accounting for radial temperature gradients were greater than those calculated from the lumped-capacity model. The fact that the three data points fall on the dashed line proves the relationship between the lumped-capacity Biot number and the radial temperature gradient Biot number is satisfied exactly. If the Biot number is determined using the simple lumped-capacity model, the correct Biot number can be calculated by finding the root of the rearranged form of eq. (10):

$$f(Bi) = 0.0373 \, Bi^3 - 0.248 \, Bi^2 + Bi - Bi_L = 0, \tag{12}$$

for values of the Biot number between 0 and 0.9, where Bi_L is the Biot number calculated using the lumped-capacity model.

Experiments 1 and 2 were almost identical, yet the Biot numbers calculated from each differ by about 4%. This difference could have been caused by a change in the position of the charge within the furnace. The lengths of the heated zones were 15 cm, not overly long compared to the charge length of 7 cm. It is possible that one or both experiments were influenced by the charge being positioned in a region where the temperature changed with height in the furnace. This would cause axial temperature gradients in the melt that would violate the assumptions of the models used. However, the small difference in Biot numbers between experiments 1 and 2 is not significant when considering the fact that heat transfer coefficients depend continuously on position in a crystal growth furnace, and this technique was used to get an overall value for the heat transfer coefficient in a zone.

The Biot number calculated from experiment 3 was about 20% higher than those calculated from experiments 1 and 2. Experiments 1 and 2 measured the heat transfer coefficient in the upper zone, while experiment 3 measured that in the lower zone. The difference in heat transfer characteristics between the upper and lower zones was unexpected. These zones are constructed identically. The temperature drops as the bottom of the

lower zone is approached. This temperature gradient caused axial heat transfer which could have increased the heat transfer coefficient.

It is also probable that natural convection was present in the liquid during the experiments. However, the effect of natural convection would not be expected to be large in a low Prandtl number fluid like a semiconductor melt.

The values of the heat transfer coefficient calculated experimentally differ by 15% from simple theoretical estimations. This difference is quite small and could be due to inaccuracies in the values of emissivity and view factor.

7. Conclusions

A practical, experimental approach was developed to determine the average heat transfer coefficient between a charge and directional solidification furnace. It was determined that the lumped-capacity model is accurate in determining the Biot number within a relative error given by eq. (10) for Biot numbers between 0 and 0.9. However, this is only if the linear regression analysis on the $\ln \theta$ versus τ plot is carried out for values of $\tau > \tau_{crit}$, where τ_{crit} is given by eq. (9). The straight line fit should not be forced through the origin because the theory that accounts for radial temperature gradients predicts a slope and a non-zero intercept. For values of $\tau > \tau_{crit}$, the Biot number can be determined exactly by obtaining Γ_1 from the slope of a $\ln \theta$ versus τ plot. This value can then be used to calculate the Biot number from eq. (7).

The heat transfer coefficient between the ampoule and the furnace was estimated by a simple formulation accounting for conduction and radiation across the air gap. Remarkably, the results differ by only 15% from the values calculated by the lumped-capacity method.

Acknowledgement

Nomenclature

A — Surface area of the charge (17.3 cm^2)

Bi — Biot number hR/k

Bi$_{eff}$ — Effective Biot number between the charge and ampoule and the furnace, $\bar{h}_{eff}R_a/k_{eff}$

Bi$_L$ — Biot number calculated by the lumped-capacity method

c_a — Specific heat capacity of the ampoule ($c_a = 1.19$ J/g · K at 1075 K for fused silica [11])

c_c — Specific heat capacity of the molten GaSb charge calculated using thermal conductivity, thermal diffusivity, and density data (for GaSb 0.328 J/g · K)

c_{eff} — Mass weighted average effective specific heat capacity of charge and ampoule combination, $c_{eff} = (\rho_c V_c c_c + \rho_a V_a c_a)/(\rho_c V_c + \rho_a V_a)$ (0.479 J/g · K for present experiments)

F — View factor from furnace wall to the ampoule (0.9 for present configuration)

h — Heat transfer coefficient (W/cm^2 · K)

$\bar{h}$ — Average heat transfer coefficient between the growth material and the furnace (W/cm^2 · K)

$\bar{h}_{eff}$ — Effective average heat transfer coefficient between the charge and ampoule and the furnace (W/cm^2 · K)

J_n — Bessel function of order n

k — Thermal conductivity (W/cm · K)

k_a — Thermal conductivity of ampoule ($2.42 \times 10^{-5}T + 4.48 \times 10^{-3}$ W/cm · K for fused silica [14], $k_a = 0.0308$ W/cm · K at $T = 1075$ K)

k_c — Thermal conductivity of the charge (0.171 W/cm · K for molten GaSb [12])

k_{eff} — Mass weighted effective thermal conductivity of charge and ampoule (0.146 W/cm · K)

L — Length of the charge (7 cm)

m — Slope of linear equation

Q — Heat flux per unit area through ampoule (W/cm^2)

R — Radius (cm)

R_a — Outside radius of ampoule (0.55 cm)

R_c — The charge radius (0.45 cm)

R_f — Inside radius of furnace (3.81 cm)

t — Time (s)

T — Temperature at time t (°C)

T_a — Ampoule temperature (°C)

T_h — Heater temperature (°C)

T_ℓ — Temperature of the lower furnace zone (°C)

T_u — Temperature of the upper furnace zone (°C)

T_0 — Initial temperature of charge (°C)

T_∞ — Steady-state temperature of charge (°C)

V_a — Volume of the section of ampoule containing the charge; $V_a = \pi L(R_a^2 - R_c^2)$ (2.2 cm^3)

V_c — Volume of the charge (4.46 cm^3)

α — Thermal diffusivity (cm^2/s)

α_c — Thermal diffusivity of charge (0.087 cm^2/s for molten GaSb [12])

α_{eff} — Effective thermal diffusivity of charge and ampoule (0.0628 cm^2/s)

Γ_n — nth eigenvalue

ϵ — Emissivity of the furnace (for Kanthal $\epsilon = 0.75$ [15])

θ — Dimensionless temperature $((T - T_\infty)/(T_0 - T_\infty))$

θ' — Dimensionless temperature calculated from eq. (8)

ρ_a — Density of ampoule wall, ($2.28 \times 10^{-4}T + 2.273$ g/cm^3 for fused silica [17], $\rho_a = 2.586$ g/cm^3 at 1075 K)

ρ_{avg} — Average density of charge and ampoule, $\rho_{avg} = (\rho_c V_c + \rho_a V_a)/(V_c + V_a)$ (4.85 g/cm^3)

ρ_c — Density of charge (5.98 g/cm^3 for molten GaSb at 800°C [16])

σ — Stefan–Boltzmann constant (5.67×10^{-12} W/cm^2 · K^4)

τ — Dimensionless time ($\alpha t/R^2$)

τ_{crit} — Dimensionless time beyond which eq. (8) is valid

τ_{eff} — Effective dimensionless time ($\alpha_{eff}t/R^2$)

References

[1] C.E. Chang and W.R. Wilcox, J. Crystal Growth 21 (1974) 135.

[2] T.W. Fu and W.R. Wilcox, J. Crystal Growth 48 (1980) 416.

[3] F.M. Carlson, A.L. Fripp and R.K. Crouch, J. Crystal Growth 68 (1984) 747.

[4] C.J. Chang and R.A. Brown, J. Crystal Growth 63 (1983) 343.

[5] R.J. Naumann, J. Crystal Growth 58 (1982) 554.

[6] P.C. Sukanek, J. Crystal Growth 58 (1982) 208.

[7] T.W. Fu, PhD Thesis, Clarkson University (1981).

[8] M.N. Ozisik, Heat Transfer; A Basic Approach (McGraw-Hill, New York, 1985).

[9] H.S. Carslaw and J.C. Jaeger, Conduction of Heat in Solids, 2nd ed. (Oxford University Press, London, 1959).

[10] W.H. McAdams, Heat Transmission, 3rd ed. (McGraw-Hill, New York, 1954).

[11] E.B. Shand, Glass Engineering Handbook, 2nd ed. (McGraw-Hill, New York, 1958).

[12] A.S. Jordan, J. Crystal Growth 71 (1985) 551.

[13] R.C. Weast, Handbook of Chemistry and Physics (CRC Press, Boca Raton, FL, 1986).

[14] Y.S. Touloukian, R.W. Powell, C.Y. Ho and P.G. Klemens, Thermophysical Properties of Matter, Vol. 2, Thermal Conductivities (IFI/Plenum Data, New York, 1970).

[15] Kanthal Corporation, Bethel, CT.

[16] V.M. Glazov, S.N. Chizherskaya and N.N. Glagoleva, Liquid Semiconductors (Plenum, New York, 1969).

[17] Y.S. Touloukian, R.K. Kirby, R.E. Taylor and T.Y.R. Lee, Thermophysical Properties of Matter, Vol. 13, Thermal Expansion (IFI/Plenum Data, New York, 1973).

Appendix C 484437 N/S

N93-15312

S3 -76

P. 6

EXPERIMENTAL OBSERVATION OF THE INFLUENCE OF FURNACE TEMPERATURE PROFILE ON CONVECTION AND SEGREGATION IN THE VERTICAL BRIDGMAN CRYSTAL GROWTH TECHNIQUE†

G. T. Neugebauer‡ and W. R. Wilcox

Chemical Engineering Department and Center for Crystal Growth in Space, Clarkson University, Potsdam, NY 13699-5700, U.S.A.

(Received 13 February 1991)

Abstract—Azulene-doped naphthalene was directionally solidified during the vertical Bridgman–Stockbarger technique. Doping homogeneity and convection were determined as a function of the temperature profile in the furnace and the freezing rate. Convection velocities were two orders of magnitude lower when the temperature increased with height. Rarely was the convection pattern axisymmetric, even though the temperature varied less than 0.1 K around the circumference of the growth ampoule. Correspondingly the cross sectional variation in azulene concentration tended to by asymmetric, especially when the temperature increased with height. This cross sectional variation changed dramatically along the ingot, reflecting changes in convection presumably due to the decreasing height of the melt. Although there was large scatter and irreproducibility in the cross sectional variation in doping, this variation tended to be least when the growth rate was low and the convection was vigorous. It is expected that compositional variations would also be small at high growth rates with weak convection and flat interfaces, although this was not investigated in the present experiments. Neither rotation of the ampoule nor deliberate introduction of thermal asymmetries during solidification had a significant influence on cross sectional variations in doping. It is predicted that slow directional solidification under microgravity conditions could produce greater inhomogeneities than on Earth. Combined use of microgravity and magnetic fields would be required to achieve homogeneity when it is necessary to freeze slowly in order to avoid constitutional supercooling.

1. INTRODUCTION

The Bridgman technique is widely used for directional solidification of metals, semiconductors, inorganic salts and organic compounds. In the Bridgman–Stockbarger manifestation, an ampoule containing the material to be solidified is slowly translated from a furnace held at a temperature above the melting point of the material into a chamber held below the melting point. In the gradient freeze mode, the ampoule is held fixed in a furnace which has a temperature decreasing continuously from one end to the other. Solidification is caused by slowly lowering the temperature of the entire furnace. In the heat exchange method, coolant is applied to one end of the ampoule. Sometimes at the same time the furnace temperature is slowly decreased.

When Bridgman crystal growth is done with the ampoule held vertically, it is normally desired that the solidification proceed upwards. Thus the temperature at the top of the apparatus is higher than at the bottom of the apparatus. For many years the crystal growth community referred to this arrangement as

"thermally stable" and many persons believed buoyancy driven convection was absent. However interest in crystal growth in space led to a closer examination of this assumption. Carlson [1] at Clarkson University and Brown [2] at MIT performed theoretical studies of convection in the Bridgman–Stockbarger technique with a step function change in temperature from the upper chamber to the lower chamber. They found that radial temperature gradients were inevitably present in the melt and could lead to vigorous convection. Initially these results were greeted with skepticism by many in the crystal growth community. Now it is widely accepted that significant convection is always present unless the operation is carried out in space or with a strong magnetic field applied to an electrically conducting melt.

By now many theoretical studies have been performed on buoyancy driven convection in the vertical Bridgman–Stockbarger technique, examining the influence of gravitation level, interface curvature, insulation thickness between the two furnaces, ampoule properties, density variations caused by variations in melt composition, varying temperatures in the heating and cooling chambers, etc. (e.g. [1–7]). Until recently [7] it was assumed that the convection was axisymmetric and steady. With one exception [5], theoretical predictions for convection have not been

---

†Paper IAF-90-358 presented at the *41st Congress of the International Astronautical Federation*, Dresden, Germany, 6–12 October 1990.
‡Present address: II-VI Inc., Saxonburg, PA 16506, U.S.A.

compared with experiment because the theoretical work was all done for metals and semiconductors opaque to light. (In Ref. [5], convection was observed in an organic compound. Measured temperatures and interface shapes were used to calculate the convection.)

Potts [8,9] performed experiments on an organic compound (high Prandtl number) heated and cooled by constant temperature baths separated by a diaphragm. The convection in the melt was neither axisymmetric nor steady, although it was very weak. While temperature variations could not be detected in the top heating bath, it was significant that the convection always rose on the side of the ampoule nearest the heater submerged in the circulating bath.

In order to see if either non-uniform heating or misalignment from vertical is necessary to cause the convection to be asymmetric, Neugebauer constructed an apparatus with vertical heating wires embedded in plastic [10,11]. The ampoule was embedded in the same plastic, so that there was no fluid between the heating elements and the ampoule. Convection was measured by taking streak photographs of small sulphur particles suspended in organic melts. Even though no circumferential variation in temperature could be measured, the convection was seldom axisymmetric. Furthermore the vertical temperature profile in the heater exerted a very strong influence on the convection in the melt. If the temperature increased with height, the convection became immeasurably small. If the temperature decreased with height, the convection was very vigorous.

The purpose of the research reported here was to determine the influence of heater temperature profile on impurity segregation and to relate this to the convection in the melt.

2. EXPERIMENTAL METHODS

The experimental methods are described in detail elsewhere [12]. Naphthalene doped with approx. 0.3% m azulene was used for the experiments. Azulene has an equilibrium distribution coefficient of about 0.3 in naphthalene [13]. The Schmidt number was estimated to be 420 [12].

The primary heater was constructed by wrapping nichrome wire around a 23 cm long Pyrex tube. An additional glass tube was put inside this tube and another outside it, all fitting together snugly. Below the primary heater was a shorter 6 cm long heater constructed in a similar fashion and with a separate power supply. Below the heaters were a layer of insulation and then a circulating constant temperature bath.

The azulene-doped naphthalene was contained in 15.6 mm i.d. Pyrex ampoules. The ingot resulting from directional solidification was transparent except near the top end. This ingot was removed from the ampoule by heating until it slid out. It was cut into sections with a saw. Samples were taken by scratching

local areas with glass capillaries, each removing about 0.1 mg of material. The samples were dissolved into acetone and the amount of naphthalene and azulene determined by gas chromatography using a flame ionization detector.

For visualization of convection, a similar apparatus was built with provision for laser slit illumination, as in Refs [10] and [11]. Convection was revealed by taking time exposure photographs of small sulphur particles suspended in salol (phenyl salicylate).

3. EXPERIMENTAL RESULTS FOR STABILIZING THERMAL CONDITIONS

By adjusting the temperatures of the two heaters a wide variety of temperature profiles were achieved. These can be classified into two categories; those in which the temperature increased with height (stabilizing) and those in which the temperature decreased with height (destabilizing). Figure 1 shows the temperature profile used for all of the solidification experiments performed under stabilizing conditions. This profile was measured with thermocouples cemented to the outer wall of the Pyrex ampoule. The radial variation in melt temperature near the solid–liquid interface was about 0.2 K, which corresponds to a Grashof number of about 10. In flow visualization experiments performed under similar conditions, significant convection was observed only near the top of the ampoule where the temperature decreased with height. In the lower portion of the ampoule the sulphur particles settled slowly, but their paths showed slight deviations from the vertical. From these deviations it was estimated that convective velocities near the solid–liquid interface were of the order of 10 μm/s.

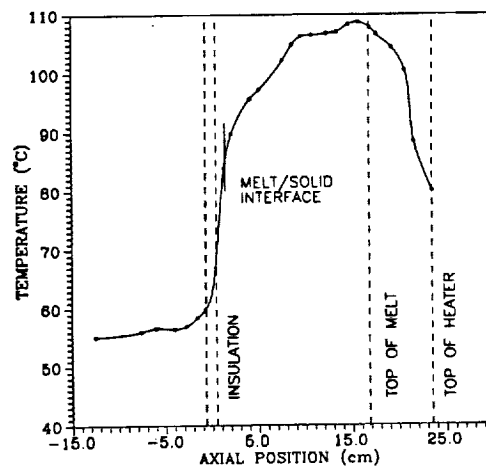Figure 2 shows the axial azulene concentration profile for a freezing rate of about 3 mm/h (0.8 μm/s),

Fig. 1. Axial temperature profile used for all growth experiments in the thermally stabilized configuration. The top of the melt position is that at the beginning of a growth run; during growth the melt level slowly falls as the ampoule is lowered.
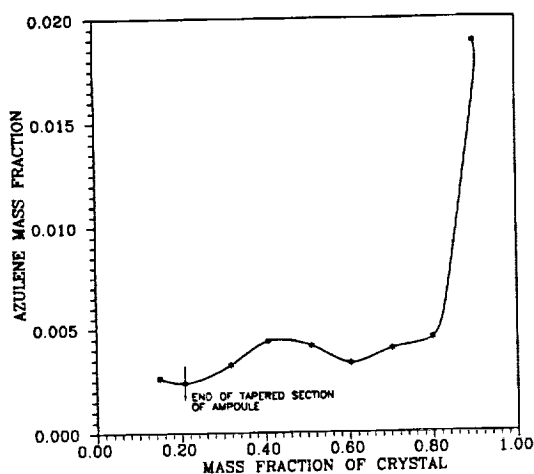
Fig. 2. Axial azulene concentration profile in a naphthalene ingot 30, which was solidified with Pe = 3.2 in the thermally stabilizing configuration.
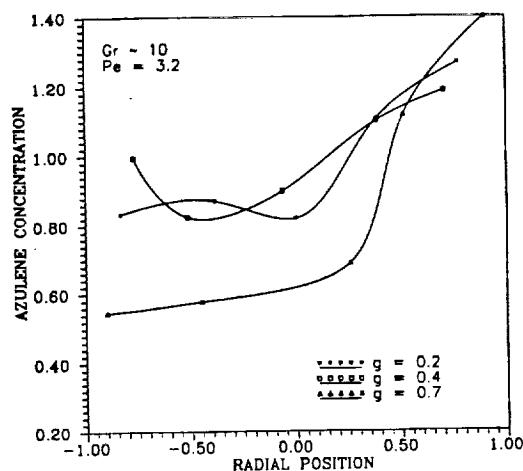

Fig. 3. Diamteric concentration profiles for the same ingot as in Fig. 2, at different axial positions. Here g is the mass fraction of the original charge that had been solidified at the position.

which corresponds to a Peclet number Pe of 3.2 ($Pe = RV/D$, where $R = 7.8$ mm and D was estimated to be 2×10^{-5} cm/s). This concentration profile is typical of what one would expect to obtain with significant convection in the melt during solidification. Figure 3 shows variations in azulene concentration along a diameter at different positions down the ingot of Fig. 2. (Here g is the mass fraction solidified.) Because the interface was nearly planar, these variations in concentration could only have been caused by convection. Since azulene is rejected by the growing naphthalene, its concentration in-

creases as the melt moves along the freezing interface. Thus we expect that convection of the melt along the freezing interface was in the direction of increasing azulene concentration in the resulting solid. In this way we can conclude from Fig. 3 that the convection was asymmetric during solidification of this material.

We define two parameters to characterize the cross sectional variation in azulene concentration and its asymmetry. The "segregation index" is defined as the absolute value of the maximum deviation in concentration from the mean, divided by the mean. Thus in Fig. 3 for $g = 0.7$ the segregation index is about 0.45.

Table 1. Results from experiments performed under the thermally stabilizing condition shown in Fig. 1

Peclet No.	Crystal	Mass fraction	Segregation	Asymmetry index
3.2	30	0.2	0.27	0.51
		0.4	0.19	0.34
		0.7	0.45	1.56
	32*	0.2	0.44	0.84
		0.6	0.11	0.17
		0.7	0.68	2.8
	53	0.2	0.13	0.13
		0.5	0.31	0.50
			0.17	0.02
5.6	35	0.6	0.22	0.05
	54	0.5	0.30	0.74
			0.49	0.76
	37†	0.3	0.64	1.1
		0.6	0.42	0.86
7.4	50	0.2	0.46	0.44
			0.29	0.20
		0.5	0.57	0.89
			0.45	0.17
	55	0.5	0.59	0.71
			0.59	0.45
8.6	34	0.4	0.45	0.21
		0.6	0.21	0.02
	49	0.2	0.29	0.06
			0.28	0.20
		0.5	0.67	1.3
			0.51	0.13

*Ampoule rotated at 2/3 rpm during solidification.
†Insulation applied to one side of apparatus to yield a temperature difference of 6.4 K across the outside of the ampoule near the solid-liquid interface.

The "asymmetry index" is defined as the maximum ratio of concentration at $+R$ to concentration at $-R$, minus 1. In Fig. 3 the asymmetry index for $g = 0.7$ is about 1.56. The segregation index would be 0 for a constant concentration, while the asymmetry index would be 0 for a completely symmetrical concentration profile.

Table 1 summarizes the results for thermal stabilizing conditions. No trends are obvious above the large scatter in values of segregation and asymmetry indices. This reflects the stochastic nature of the convection pattern produced in each experiment. Note that segregation and asymmetry changed dramatically down each ingot, reflecting the change in convection pattern during solidification.

One would expect that at sufficiently high freezing rates the mass transfer in the melt would become diffusion controlled, causing the segregation and asymmetry indices to decline and approach the values expected for diffusion controlled conditions. Although the data suggest there may be a maximum in segregation index at a Peclet number of about 7, there is too much scatter to be certain.

Thermocouple measurements around the outer wall of the ampoule in these experiments showed no circumferential variation in temperature, within a sensitivity of 0.1 K. It is commonly believed that a constant temperature circumferentially must yield axisymmetric convection and impurity concentration patterns. Therefore an experiment was performed in which the ampoule was rotated at 2/3 rpm, in order to further reduce any circumferential variation in temperature. As shown in Table 1, the segregation and asymmetry indices were unchanged, within experimental scatter (which was large). Similarly, insulating one side of the heater to deliberately produce an asymmetric temperature field did not significantly increase the segregation and asymmetry indices.
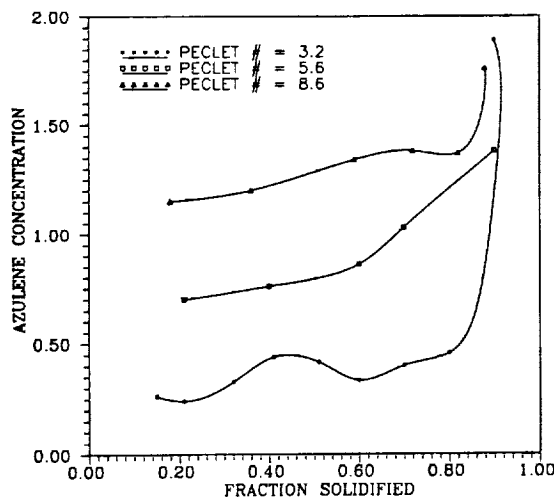

Fig. 5. Typical axial temperature profile for thermally destabilizing condition. Based on the temperature difference between the maximum and the top of the melt, the Grashof number is estimated to have been 158,000.

Axial concentration profiles also reflect the intensity of convection. Figure 4 shows such profiles for three different freezing rates. The concentration profile at Pe = 3.2 is characteristic of convection-controlled mass transfer. As Pe was increased, the azulene concentration in the first 80% of the ingots increased significantly, indicating the decreasing influence of convection.

4. EXPERIMENTAL RESULTS FOR DESTABILIZING THERMAL CONDITIONS

Figure 5 shows a typical destabilizing temperature profile. This profile was measured by a fine thermocouple inserted into the melt. Convection was vigorous throughout the ampoule, and was rarely

Fig. 4. Axial concentration profiles for ingots solidified at three different rates under the thermally stabilizing condition.

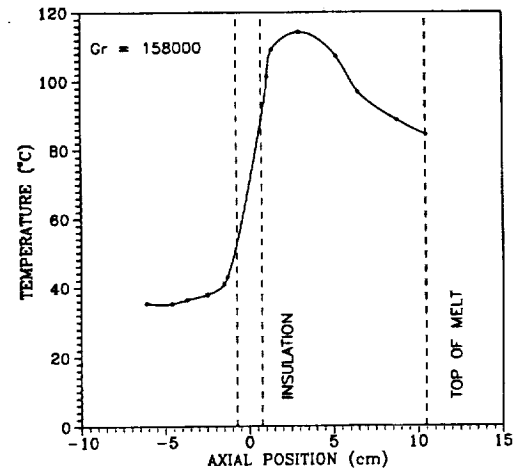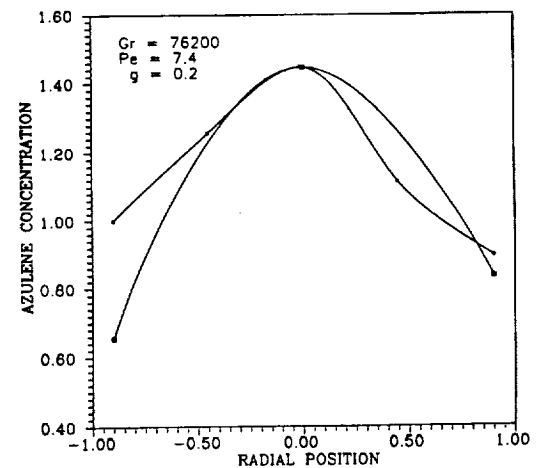Fig. 6. Concentration profiles along two perpendicular diameters at the position where 20% of the melt had been solidified. Ingot 51 with destabilizing thermal conditions, Gr = 76,200 and Pe = 7.4.

Table 2. Results from experiments performed under thermally destabilizing conditions

Peclet No.	Crystal	Grashof No.	Mass fraction	Segregation	Asymmetry index
3.2	41	55,600	0.5	0.05	0.05
	42	88,500	0.2	0.93	0.07
				0.93	0.22
			0.5	0.04	0.02
				0.04	0.03
	43	116,000	0.5	0.04	0.04
5.6	44	39,600	0.5	0.17	0.36
	45	121,000	0.5	0.07	0.08
				0.07	0.07
7.4	51	76,200	0.2	0.45	0.13
				0.25	0.27
			0.5	0.14	0.18
				0.26	0.68
	52	138,000	0.5	0.13	0.13
				0.12	0.07
8.6	47	76,700	0.5	0.21	0.46
	48	109,000	0.2	0.47	1.2
			0.5	0.50	0.61
				0.50	0.38
	46	158,000	0.5	0.15	0.35

axisymmetric. The convection velocities were on the order of 1 mm/s, or about 100 times larger than with a stabilizing profile. The convection increased as the temperature gradient was increased. The temperature gradient was characterized by a Grashof number that used the temperature difference between the temperature in the melt and the temperature at the upper surface of the melt measured when the top of the melt was 10.5 cm above the insulated zone, corresponding to $g = 0.2$.

Figures 6 and 7 show typical cross sectional variations in azulene concentration. Visually the diametric concentration profiles often appeared nearly symmetrical, sometimes with a maximum near the center and other times with a minimum. As in the stabilizing configuration, the concentration profiles changed dramatically down each ingot.

As shown in Table 2, the segregation and asymmetry indices again showed a great deal of scatter, but tended to be smaller than with thermally stabilizing

conditions. The asymmetry appeared to be smallest when Pe was small and Gr was large (low growth rate with vigorous convection).

5. IMPLICATIONS FOR SOLIDIFICATION IN SPACE

A common justification for use of microgravity in directional solidification is that more uniform doping levels should be obtained. However the present results show that under some conditions inhomogeneities could be greater in space than on Earth. In microgravity, weak buoyancy-generated convection will occur. If this weak convection is combined with low freezing rates, greatly increased inhomogeneities could result. Thus when low freezing rates are necessary in order to avoid constitutional supercooling, it may be necessary to combine microgravity and magnetic fields in order to achieve homogeneous crystals.

Fig. 7. Concentration profiles along two perpendicular diameters in the same ingot as Fig. 6, except at the position where 50% of the melt had been solidified.

REFERENCES

1. L. Y. Chin and F. M. Carlson, *J. Crystal Growth* **62**, 561 (1983).
2. C. J. Chang and R. A. Brown, *J. Crystal Growth* **63**, 343 (1983).
3. F. Carlson, private communication, Clarkson University (1990).
4. P. M. Adornato and R. A. Brown, *J. Crystal Growth* **80**, 155 (1987).
5. L. C. Tien and J. O. Wilkes, in *Heat Transfer, Volume 1, Heat Exchangers* (Edited by U. Grigull and E. Hahne). Elsevier, Amsterdam (1970).
6. M. J. Crochet, F. Dupret, Y. Ryckmans, F. T. Geyling and E. M. Monberg, *J. Crystal Growth* **97**, 173 (1989).
7. W. Arnold, D. Jacqmin, R. Gaug and A. Chait (NASA-Lewis), *28th AIAA Aerospace Sciences Meeting*, Reno, Nev. (1990).
8. H. Potts, M.S. thesis, Clarkson University (1984).
9. H. Potts and W. R. Wilcox, *J. Crystal Growth* **74**, 434–445 (1986).

10. G. Neugebauer, M.S. thesis, Clarkson University (1986).
11. G. Neugebauer and W. R. Wilcox, *J. Crystal Growth* **89**, 143–154 (1988).
12. G. Neugebauer, Ph.D. thesis, Clarkson University (1989).
13. N. Karl, in *Crystals: Growth, Properties and Applications.* Springer, New York (1981).

AIAA 92-0353

Influence of the Accelerated Crucible Rotation Technique on Directional Solidification of InSb-GaSb Alloys

R.T. Gray and W.R. Wilcox
Center for Crystal Growth in Space
Clarkson University
Potsdam, NY 13699

30th Aerospace Sciences Meeting & Exhibit
January 6-9, 1992 / Reno, NV

INFLUENCE OF THE ACCELERATED CRUCIBLE ROTATION TECHNIQUE ON DIRECTIONAL SOLIDIFICATION OF InSb-GaSb ALLOYS[1]

R.T. Gray and W.R. Wilcox
Center for Crystal Growth in Space
Clarkson University
Potsdam, NY 13699

Abstract

The objective of this research was to determine the influence of the accelerated crucible rotation technique (ACRT) on the directional solidification of $In_xGa_{1-x}Sb$ alloys. Ingots of $In_xGa_{1-x}Sb$ were solidified with application of ACRT using different rotation rates and cycle times and without application of ACRT. The vertical Bridgman-Stockbarger growth technique was used. No significant radial segregation was found in any of the ingots grown with or without application of ACRT. The axial composition profiles of all ingots suggest that the melt was well-mixed during solidification. Application of ACRT using a rotation rate of 80 rpm consistently led to fewer grain and twin boundaries than ingots solidified without application of ACRT. These conditions led to a 19% reduction in the number of twin boundaries and a 32% reduction in the number of grain boundaries.

Introduction

Bulk, single crystals of alloy systems such as $In_xGa_{1-x}Sb$ would have many possible applications, such as photodetectors and microwave oscillators [1-3]. Alloy systems offer the advantage of having a composition dependent band structure that allows one to vary the crystal properties to suit different applications. Sizeable single crystals with compositional homogeneity and low defect densities are needed for applications.

Experimenters have tried many different methods of growing bulk crystals of III-V alloys. Almost every attempt has resulted in polycrystalline and/or compositionally inhomogeneous solids that are not suitable for devices. A major cause for the lack of success in growing bulk alloys is the extensive segregation that occurs due to the breadth of the two-phase region on the equilibrium phase diagram. For example, the pseudo-binary phase diagram for the InSb-GaSb system is shown in figure 1 [4]. The rejection of InSb during directional solidification results in its buildup in the melt adjacent to the interface. This can lead to
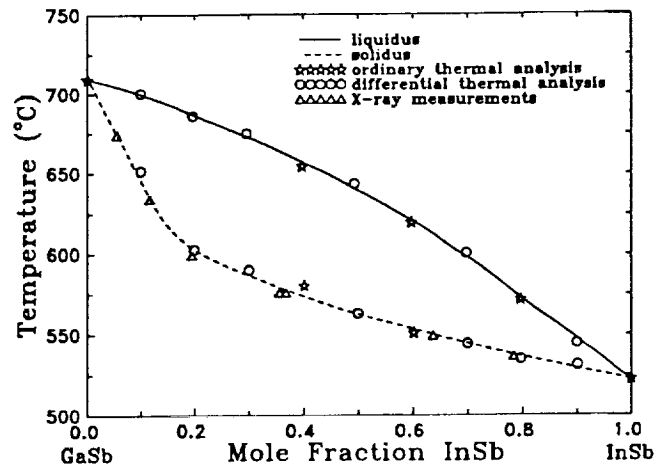

Figure 1: Pseudo-binary phase diagram for the InSb-GaSb alloy system [4].

constitutional supercooling [5-9] at high growth rates or at low imposed temperature gradients.

The vertical Bridgman-Stockbarger technique is a method of directional solidification that is both well-studied and popular. It has been used to solidify ingots of many different concentrated alloy systems including $In_xGa_{1-x}Sb$ [10], $Cd_xHg_{1-x}Te$ [11-20], $Cd_xHg_{1-x}Se$ [21], and $Zn_xHg_{1-x}Te$ [22]. In the vertical Bridgman-Stockbarger technique, the charge is sealed in a growth ampoule and lowered at a slow rate through a temperature gradient created by a higher temperature furnace on top of a lower temperature furnace. This set-up allows one to control the interface shape, growth rate, and temperature gradient independently. While this arrangement, with the higher temperature on top, is said to be thermally stable, natural convection will always be present on earth due to unavoidable radial temperature gradients and variations in composition. This convection is often time-dependent [23]. The result is variations in temperature and flow velocity near the interface, causing growth rate fluctuations. An inhomogeneous composition profile with striations parallel to the interface can develop.

One possible way to eliminate the problems associated with time-dependent free convection is to suppress the convection. This could be accomplished by applying a magnetic field to the melt (if it is an

1

electrical conductor) [10] and/or by carrying out the solidification in space [24-28]. Another approach is to introduce regular, forced convection on a scale that overwhelms any natural convective effects. Using forced convection offers the additional advantage of keeping the melt well-mixed, eliminating cross-sectional compositional variations. It is difficult to stir the melt because of the impracticality of placing a mechanical device inside the growth ampoule. A stirrer would be a source of impurities. Also, the material must be totally sealed in an inert atmosphere or vacuum to prevent escape of volatile components and to keep the melt from reacting with air.

Spin-up/spin-down [29,30], often called the accelerated crucible rotation technique (ACRT) when applied to crystal growth [11,15-18,31-37], is a method by which effective mixing can be obtained without making physical contact with the melt. Mixing is accomplished by periodically varying the rotation rate of the ampoule. Capper et al. [11] at Philips in Southampton, England applied ACRT during the vertical Bridgman growth of $Cd_xHg_{1-x}Te$. They got a drastic improvement in compositional homogeneity and crystal grain size over material solidified without ACRT.

Recent research by Larrousse and Wilcox [38,39] at Clarkson University suggests that ACRT leads to large fluctuations in freezing rate and segregation. Meltback of the grown solid might even occur during each spin-up/spin-down cycle. This periodic melting and freezing could have enhanced grain selection and eliminated twins in the solidification of $Cd_xHg_{1-x}Te$ at Philips. The benefit of periodic melting and freezing was shown by Jackson and Miller [40] using the organic compound salol. Another possible explanation for the improved crystalline perfection of the ingots grown with ACRT is that ACRT causes the interface to be less concave (more convex) [15]. This would enhance grain selection by causing grains not aligned with the direction of growth to grow out as solidification proceeds.

Objectives

The objective of this work was to determine the influence of ACRT on the vertical Bridgman-Stockbarger solidification of $In_xGa_{1-x}Sb$ ingots. Both the microstructure of the ingots and their compositional homogeneity were investigated. After determining how ACRT affected the $In_xGa_{1-x}Sb$ ingots, this information was used to propose a mechanism by which the marked improvements in grain structure came about.

Experimental Procedures

Ampoule and Materials Preparation

Fused silica (quartz) ampoules were used to hold the growth materials during solidification. The ampoules had an inside diameter of 9 mm and an outside diameter of 11 mm. One end of each tube was sealed so the ampoule resembled a long test tube (one end with a domed shape). The ampoules were cleaned thoroughly by rinsing in aqua regia (3 parts HCl to 1 part HNO_3 by volume), a 10% HF solution, and deionized water.

The starting materials were six nines purity indium, gallium, and antimony. These materials were weighed to an accuracy of ±0.005 g to give a starting composition of 20 mole % InSb ($In_{0.2}Ga_{0.8}Sb$) and an ingot length of approximately 7 cm. Before the ingots were solidified, the starting materials were compounded, sandblasted, and ultrasonically cleaned in methanol.

The pure elements were loaded into an ampoule, an 8 mm quartz plug was placed 25 cm from the bottom of the ampoule, and it was evacuated using a cryogenic vacuum pump. The ampoule was flushed five times with ultra-high purity argon to aid in the removal of oxygen and was left on the vacuum system for 12 to 16 hours. It was then sealed at a pressure of 10^{-6} torr by fusing the quartz ampoule to the plug with a hydrogen-oxygen torch.

Compounding and mixing of the pure elements was carried out in a rocking furnace built specifically for mixing molten materials. The 25 cm long ampoule containing the pure elements was placed in the furnace, which was then heated rapidly to 800°C. The rocking motion was started, and continued for 6 hours. After rocking was stopped, the furnace was placed manually to the horizontal position to place the molten charge in the center of the ampoule. The furnace power was then turned off. This often caused the ampoule to break and the $In_{0.2}Ga_{0.8}Sb$ charge to oxidize.

The $In_{0.2}Ga_{0.8}Sb$ removed from the rocking furnace always had a black, charcoal-like scum on its surface, even when the ampoule did not break during solidification. This scum was removed by sandblasting the $In_{0.2}Ga_{0.8}Sb$ at 10 psig pressure with 220 grit SiC particles. The material was then ultrasonically cleaned for 5 minutes in electronic grade methanol.

The $In_{0.2}Ga_{0.8}Sb$ charge was ready to be sealed in a growth ampoule and directionally solidified. The charge was slid into a 56 to 60 cm long quartz ampoule that had been cleaned according to the procedure described above. The ampoule was evacuated and sealed about 20 cm from the bottom of the ampoule. The procedures used were exactly as explained

2

Figure 3: Accelerated crucible rotation technique program used for all experiments.

Figure 2

Figure 2: Schematic diagram of the vertical Bridgman-Stockbarger growth furnace.

above. The ampoule was then ready to be placed in the vertical Bridgman-Stockbarger growth apparatus.

Bridgman-Stockbarger Growth Apparatus

The directional solidification for the ACRT experiments was carried out in a vertical Bridgman-Stockbarger furnace shown schematically in figure 2. Both the hot and cold zones were Kanthal wound resistance heaters. The 30.5 cm long hot zone and 15.2 cm long cold zone were separated from one another by a 6.4 cm thick adiabatic zone. The adiabatic zone consisted of 23 cm diameter zirconia insulating disks. A 29 mm diameter quartz tube was used as a liner. This ran through the center of the entire apparatus.

An aluminum mounting bracket was attached to the translation mechanism. This bracket held a gearmotor that was used to provide the rotation necessary for ACRT. Ampoule rotation was stopped and started by turning the gearmotor on and off using a laboratory timer.

Vertical Bridgman-Stockbarger Solidification

The hot zone temperature was chosen to be 800°C and the cold zone 480°C. To begin each growth experiment, the bottom of the ampoule was placed above the adiabatic zone. The hot zone was heated to 800°C and the cold zone to 480°C. Periodic rotation of the ampoule was then started and continued
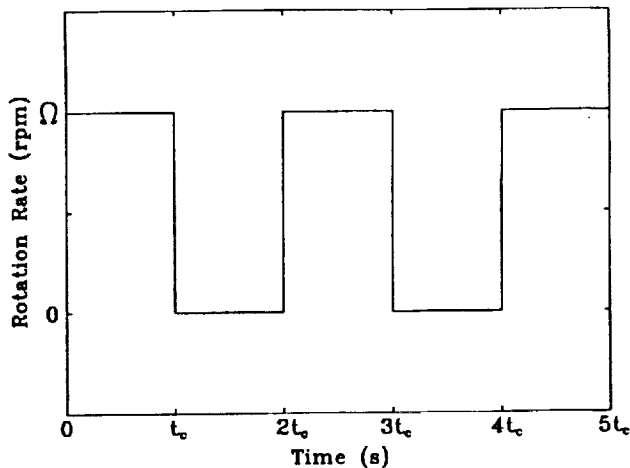
for 2 to 3 days to mix the material prior to growth. The rotation rate Ω used was 80 rpm and the cycle time t_c was 26.5 s. The rotation rate program used in all experiments is shown in figure 3. It consisted of spin-up from rest and spin-down to rest. The rotation rate was impulsively changed from 0 rpm to the value of Ω rpm and held there for the time t_c. The rotation rate was then stopped and held at 0 rpm for the time t_c. This cycle was continuously repeated.

After solidification the ingots were sliced longitudinally and cut into sections for analysis. They were mounted in epoxy resin and polished to flat surfaces by rough grinding and fine polishing. The final polishing step used a suspension of 0.5 micron alumina particles in distilled water.

Compositional Analysis

Energy-dispersive X-ray spectroscopy (EDX) was used to measure the composition of the polished samples. The spectrometer was used with the ISI Scanning Electron Microscope at Clarkson University. The mole fraction of InSb x_s in the unknown sample was determined using a method developed for $Cd_xHg_{1-x}Te$ at the NASA Marshall Space Flight Center [41].

To determine the radial segregation in the ingots, data were gathered at 1 mm intervals across the radius of the longitudinal sections. This was done at various axial locations in the ingots. X-ray data were collected at spacings of 1 to 2 mm along the center of the longitudinal sections to find the axial composition profile of the ingots. The data were plotted as the mole fraction of InSb x_s versus the mole fraction of ingot solidified g.

The axial position z in the ingots had to be converted to mole fraction solidified g. Our ingots were

3

not perfectly cylindrical over their entire length and the total molar concentration of the solid changed by almost 17% over the length of the ingot. The relationship between the mole fraction solidified and the axial position in the ingot is:

$$g = \left(\int_0^z \bar{C}_s A_c dz \right) / \left(\int_0^L \bar{C}_s A_c dz \right), \quad (1)$$

where A_c is the cross-sectional area of the ingot at position z, $\bar{C}_s$ is the total molar concentration of the solid at position z, and L is the total length of the solidified ingot. Both the bottoms and tops of the directionally solidified ingots had dome shapes. It was assumed that the bottoms and tops were half-ellipsoids to relate A_c to z. The variation in total molar concentration of the solid with mole fraction InSb x_s in the solid was calculated using the variation of lattice spacing a with x_s. Woolley and Smith [42] reported this to be:

$$a = 6.1 \times 10^{-8} + 3.9 \times 10^{-9} x_s \ (\text{cm}). \quad (2)$$

Knowing the lattice spacing, the total molar concentration can be calculated using the relationship:

$$\bar{C}_s = 4/(N_A \cdot a^3), \quad (3)$$

where 4 is the number of molecules per unit cell and N_A is Avogadro's number (number of molecules per mole). The value of x_s was already known at specific axial locations from the EDX measurements. If a value was needed for $\bar{C}_s$ at axial locations where the composition x_s was not measured, the composition at this point was estimated using linear interpolation. The corresponding value of $\bar{C}_s$ could then be determined from equations (2 and 3).

Microstructural Analysis

The numbers of grain boundaries and twin boundaries in the ingots were used to quantify their microstructure. In order to reveal these boundaries, the polished samples were chemically etched. This was done by lowering them for 6-10 seconds into 240 ml of a mixture of 1 HF:1 HNO$_3$:1 H$_2$O by volume. The samples were then removed and rinsed immediately in deionized water followed by methanol. This procedure clearly revealed grain and twin boundaries in the ingots. Adjacent grains and twins in the samples were clearly visible with the naked eye under fluorescent lighting. Some grains and twins appeared bright, while others were dark. This depended on the angle of the incident light. Figure 4 shows how a typical sample appeared under fluorescent lighting.

Optical microscopy at a magnification of 200X was used to count the number of grain and twin boundaries in the ingots. At this magnification, all

Figure 4: Photograph of In$_x$Ga$_{1-x}$Sb sample under fluorescent lighting. (The width of the sample is 9 mm).

boundaries in the samples could be distinguished individually. The samples were viewed using polarized light with a 1/4-wave plate in a Nikon Optiphot-2 microscope. The 1/4-wave plate caused the samples to appear in color instead of black-and-white. Adjacent grains and twins were different colors. The color of a particular grain or twin changed as the direction of the polarized light was rotated. The color of a grain or twin depended solely on its orientation.

Considerable difficulties were encountered when trying to distinguish grain boundaries from twin boundaries. Twin boundaries have been observed to kink on a microscale to give the appearance of being curved [26]. This prohibits the positive identification of a boundary as a grain boundary just because it appears curved under the optical microscope. In this work, many observations were used to distinguish grain boundaries from twin boundaries. Following is a list of some of the attributes of grain boundaries and twin boundaries in the etched samples:

1. Grain boundaries tended to be much wider and deeper than twin boundaries due to the larger amount of mismatch between adjacent grains. They usually were more irregular.

2. Many twin boundaries were easily recognizable because they had perfectly straight edges and were parallel to one another when in the same grain. Parallel twins in the same grain could also be recognized because of the alternation between the same two colors across the boundaries. This means that the orientation returned to its original value when two twin boundaries were crossed. Alternation between colors could also be used to classify twin boundaries that appeared curved.

3. Some twin boundaries were kinked on a scale

large enough to be seen easily at 200X. Other twin boundaries had long sections that were perfectly straight. These sections might have been connected by sections that appeared curved. In these cases, it was inferred that the curved sections were actually kinked. Therefore, in order to classify a boundary correctly, one had to scan along its entire length.

Using the above guidelines, it is believed that over 90% of the boundaries could be classified accurately.

The numbers of grain and twin boundaries were counted at 2 mm intervals down the length of each ingot. A scan was made across the radius of the ingot at each axial location with the optical microscope. Every boundary that was intersected was counted as either a grain boundary or a twin boundary. The number of boundaries was divided by the length scanned to get a per millimeter value. The mean numbers of boundaries per millimeter in each pair of ingots were compared using a one-sided Student's t-test with paired comparisons [43,44]. Each ingot was compared with every other ingot using this technique. The probability of the number of boundaries per millimeter in one ingot being greater than that in another was determined. Paired comparisons were used because the number of twin or grain boundaries in the ingots depended not only on the method by which the ingots were solidified, but also on the axial location in the ingot. Counts of the boundaries in one ingot were paired with the counts for another ingot at the same value of mole fraction solidified g.

Interface Demarcation

The effect of ACRT on the shape of the solid/melt interface needed to be determined. Quenching the remaining melt by turning off the power to both the hot and cold zones after a portion of the ingot had been solidified gives the shape of the interface at only one location during growth. This technique was not used due to the amount of time necessary to get only one interface position and shape. Instead, a method was developed to reveal the shape of the solid/melt interface at many locations in the ingot. The procedure used to put interface striations in an ingot during solidification was: (1) The temperature of the hot zone was lowered by 50°C. (2) The temperature was kept at this level for 5 minutes. (3) While the temperature was constant, the ampoule was moved down 1 mm into the furnace. (4) The temperature of the hot zone was raised back up to the normal setpoint.

After most of an ingot was solidified, power to both furnace zones was shut off and the remainder of the melt was quenched. The ingot was removed from the furnace. It was sliced, mounted, and polished. The etching procedure used to reveal the interface

Table 1: Experimental conditions used to solidify ingots E1 to E9. The variable x is the starting mole fraction of InSb, Ω is the ACRT rotation rate, t_c is the ACRT cycle time, $\bar{V_t}$ is the average translation rate, and L is the total length of solidified ingot.

Ingot	x	Ω (rpm)	t_c (s)	$\bar{V_t}$ (mm/day)	L (mm)
E1	0.2000	0	-	8.0	70
E2	0.2000	80	10	8.2	76
E3	0.2000	16	26.5	8.1	58
E4	0.2000	50	6.4	8.1	72
E5	0.2000	0	-	-	67
E6	0.2000	80	26.5	7.9	62
E7	0.2000	50	26.5	8.3	71
E8	0.2000	200	6	8.4	70
E9	0.2000	0	-	-	69

striations was the same as that used to reveal grain and twin boundaries.

Results

Three ingots were solidified without application of ACRT and six ingots were solidified using a different combination of rotation rates Ω and cycle times t_c. The important parameters used in solidifying the nine ingots are shown in table 1.

Ingots E2, E3, E5, and E7 each had a region about 5 to 10 mm from the top of the ingot where the diameter of the ingot was less than that of the ampoule. This small section of ingot seemed to have solidified without contact with the ampoule wall. This phenomenon is similar to that seen in $In_xGa_{1-x}Sb$ ingots solidified in space in Skylab-3 [13,14]. This was described in section 2.5.3. Regel [45] suggested that it only occurs when the variation in gravity level (g-jitter) is low. Perhaps the ingots solidified under earth's gravity pulled away when the hydrostatic pressure in the melt could be overcome by the surface tension of the melt. Any fluctuation in the fluid flow, temperature, or surface composition of the melt could cause the liquid column to collapse and contact the wall at a later time. The strongest example of an ingot having a smaller diameter than the ampoule occurred in ingot E4. A large region about 2 cm from the top of the ingot had a wavy and irregular surface. This ingot appeared to have very little oxide near the top compared to other ingots.

Axial Composition

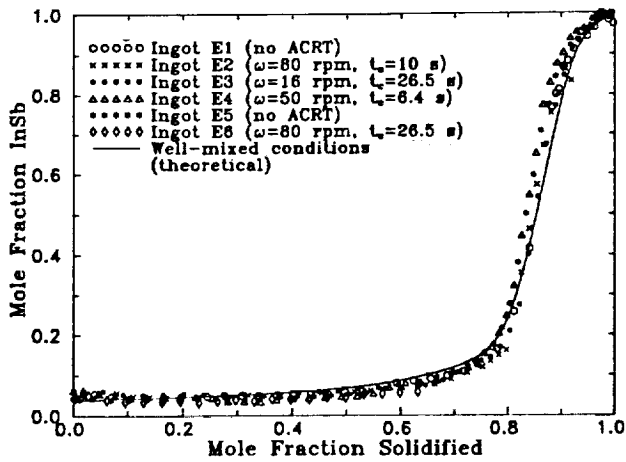Energy-dispersive X-ray spectroscopy (EDX) was used to measure the axial composition profiles for

Figure 5: Composition of InSb in the solid x_s versus mole fraction solidified g for ingots E1 to E6. The solid line is the theoretical curve for a well-mixed melt computed from equation (4).

Figure 6: The radial variation in mole fraction of InSb for different values of mole fraction solidified g in ingot E4.

ingots E1 to E6. The results are plotted in figure 5. The solid line in the figure is a theoretical curve that describes the composition profile expected in a solid that is solidified from a melt that is always completely mixed (no composition gradients exist in the melt) with equilibrium at the interface. Since the equilibrium distribution coefficient k changes with composition in the $In_xGa_{1-x}Sb$ system, this variation had to be accounted for. The equation describing the composition profile in a solid solidified from a completely mixed melt is:

$$g = 1 - \exp\left\{ -\int_{x_o}^{x_l^f} \frac{dx_l}{x_l\,[1 - k(x_l)]} \right\}, \qquad (4)$$

where x_l is the mole fraction of InSb in the melt, x_o is the initial mole fraction of InSb in the charge (0.2 here), and x_l^f is the mole fraction of InSb in the melt when the mole fraction g of the initial charge is solidified. The variation in the equilibrium distribution coefficient $k(x_l) = x_s/x_l$ with liquidus mole fraction x_l, where x_s is the mole fraction of InSb in the solid, was determined graphically from the pseudo-binary phase diagram of the InSb-GaSb system (figure 1).

The plot of mole fraction InSb in the solid x_s versus mole fraction solidified g in figure 5 shows that all six ingots had the same axial composition profile. Furthermore, all ingots were solidified from completely mixed melts. The application of ACRT had no effect on the shape of the composition profile. The agreement between the experimentally determined composition and the theoretical curve was extremely good.

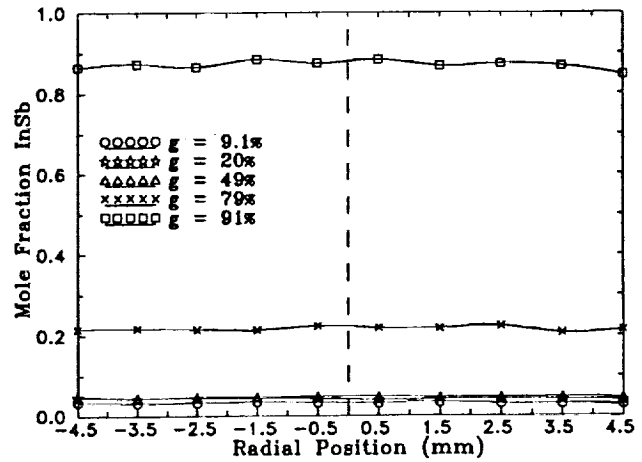## Radial Composition

Energy-dispersive X-ray spectroscopy (EDX) was used to measure the variation in composition across the radius of ingots E1 to E6. Data were collected at 1 mm intervals across the radius of the ingots at several axial locations. There was no significant radial segregation in the ingots. Figure 6 shows the radial segregation in ingot E4. The radial composition variations in ingot E4 were typical.

Microstructure

The grain structure in the first-to-freeze end of each ingot was a result of the random nucleation that occurred there. Many small, randomly oriented grains were in this region. After a distance of about one ampoule diameter (9 mm), a transition to columnar growth was seen. The most favorably oriented grains dominated. Most grains that existed after the first centimeter of growth tended to remain for the entire length of the ingot. This suggests that the interface shape was close to planar. Also, many more twin boundaries existed than grain boundaries in all ingots. The twin boundaries appeared straight over most or all of their length.

Statistical analysis on the number of twin boundaries in ingots E1 to E9 revealed that ingot E7 had the fewest number of twin boundaries. Ingots E2, E4, and E6 also had few twin boundaries compared to the other ingots. Thus, the ingots with the fewest number of twin boundaries were solidified using rotation rates of 50 rpm and 80 rpm. Ingot E1 was the first to be solidified and E9 was the last. Both ingots were solidified without application of ACRT and had the same number of twin boundaries. Ingot E5 was also solidified without ACRT, but had an unusually high number of twin boundaries. The reason for this is unknown. Ingot E8, solidified using a rotation rate of 200 rpm, had a large number of twin boundaries.
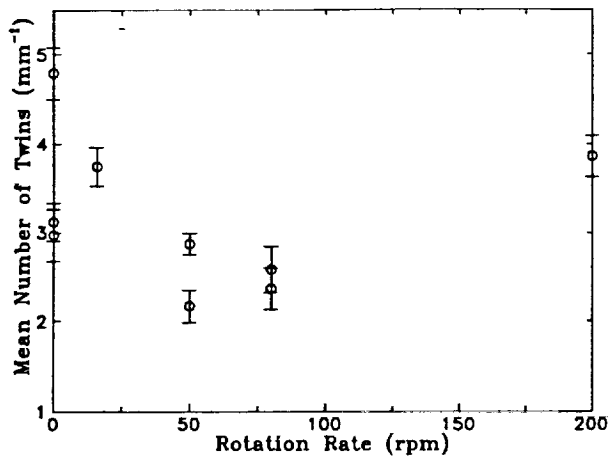
Figure 7: The mean number of twin boundaries per millimeter versus the ACRT rotation rate. The error bars represent plus or minus the standard error of the mean. A rotation rate of 0 rpm means that ACRT was not applied.
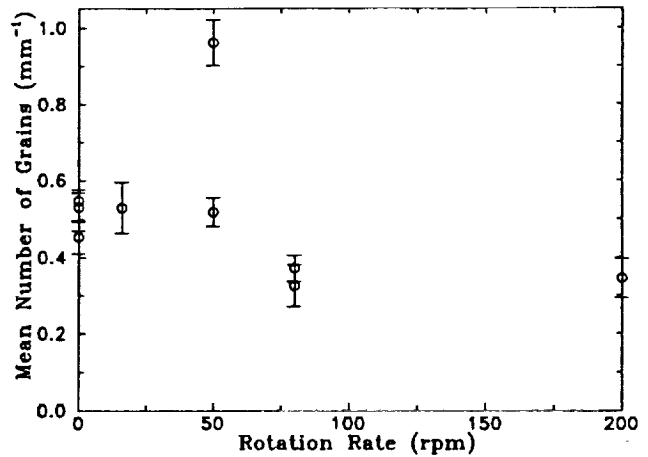

Figure 8: The mean number of grain boundaries per millimeter versus the ACRT rotation rate. The error bars represent plus or minus the standard error of the mean. A rotation rate of 0 rpm means that ACRT was not applied.

The results of the statistical analysis on the number of grain boundaries in ingots E1 to E9 showed that ingots E2, E6, and E8 had the fewest number of grain boundaries. Ingots E2 and E6 were solidified using a rotation rate of 80 rpm and had the same number of grain boundaries. Ingot E8 was solidified using a rotation rate of 200 rpm. The number of grain boundaries in ingots E1 and E9 (solidified without ACRT) was the same. Ingot E5 had fewer grain boundaries than either of these ingots, despite being solidified under the same conditions. Ingot E4 had an unusually high number of grain boundaries.

The mean number of twin and grain boundaries were plotted against the ACRT rotation rate in figures 7 and 8. The error bars in these plots represent plus or minus the standard error of the mean. The standard error of the mean is $\sigma/\sqrt{n}$, where σ is the standard deviation and n is the number of boundary counts. A rotation rate of 0 rpm means that ACRT was not applied. Figure 7 shows that the fewest number of twin boundaries existed in the ingots solidified at 50 rpm and 80 rpm. If ingot E5 is ignored because of its high number of twin boundaries compared to the other two ingots solidified without ACRT, the average reduction in the number of twins using a rotation rate of 80 rpm was 19%. There was no reduction in the number of twin boundaries when a rotation rate of 16 rpm or 200 rpm was used.

Figure 8 is a plot of the mean number of grain boundaries versus ACRT rotation rate. All three ingots solidified without application of ACRT had approximately the same number of grain boundaries. There was no reduction in the number of grain boundaries when rotation rates of 50 rpm and less were

used. The average reduction in the number of grain boundaries using rotation rates of 80 rpm and 200 rpm was 32%.

No significant effect of the ACRT cycle time on the number of boundaries in ingots E1 to E9 could be found. Only ingots solidified using rotation rates of 50 rpm and 80 rpm were solidified with two different cycle times. The results were both conflicting and statistically insignificant.

Interface Demarcation

The results of interface demarcation studies showed that application of ACRT using a rotation rate of 80 rpm and a cycle time of 10 s reduced the interface depth from 0.6 mm to 0.3 mm. The depth was defined as the average location of the interface at the ampoule wall minus the location of the interface at the position of maximum depth.

Discussion

Axial Composition

The axial composition profiles for all ingots agreed with that expected if they had grown from a melt containing no composition gradients. The first conclusion that this leads to is that free convection mixed the melt thoroughly in the ingots grown without application of ACRT. However, diffusion alone can completely mix a melt when the characteristic diffusion length ($L_D = D/V$, where D is the diffusivity of the solute in the melt and V is the growth rate) is greater than the total length of the ingot L [46]. The diffusivity of InSb in molten $In_xGa_{1-x}Sb$

is not known. If the growth rate is assumed equal to the translation rate (8 mm/day) and the length of the ingot is 7 cm, a diffusion coefficient of 6.5×10^{-5} cm^2/s is needed to make $L_D = L$. This diffusion coefficient is well within the range typical of semiconductor melts [12,21,22,36,47]. It is not surprising that the application of ACRT did not change the axial composition profile in any of the ingots. Well-mixed conditions in the melt existed without application of ACRT. Addition of forced convection would stir the melt, but this stirring could not lead to a change in the axial composition profile.

Radial Composition

No significant radial segregation was found in any of the ingots solidified with or without application of ACRT. The fact that ACRT did not create radial segregation is encouraging since Larrousse and Wilcox [38,39] showed that the mass transfer created by ACRT is not uniform radially. The absence of radial segregation without application of ACRT suggests that the interface was nearly planar throughout growth. This was confirmed using interface demarcation.

Microstructure

Grain Boundaries. The fewest number of grain boundaries existed in ingots solidified with application of ACRT using rotation rates of 80 rpm and 200 rpm. These ingots had 32% fewer grain boundaries than ingots grown without application of ACRT. Ingots E1, E5, and E9 were solidified without using ACRT. Ingot E1 was the first ingot solidified and ingot E9 was the last. The difference in the number of grain boundaries in ingots E1 and E9 was found to be statistically insignificant. This suggests that the results are repeatable from ingot to ingot. Ingot E5 had fewer grain boundaries, but figure 8 shows that the difference in the number of grain boundaries between ingots E1, E5, and E9 was small.

Grain boundaries tend to propagate in a direction approximately perpendicular to the solid/melt interface [48]. This means that the interface shape determines the grain selection process. If the interface is convex, grain boundaries will tend to grow into the ampoule walls and disappear [49,50]. A concave interface will cause grains to grow in toward the center of the ampoule. Thus, grains that nucleate at the wall of the ampoule grow inward, deteriorating the microstructure of the ingot [51]. When the interface is approximately planar, grains that exist at the beginning of the ingot would tend to remain throughout the entire ingot. Most grains in ingots E1 to E9 tended to remain throughout the entire ingot. This and the lack of radial segregation in ingots E1 to E6 suggest that the interface shape was nearly planar

during the growth of all ingots. This was confirmed by the interface demarcation studies. The interfaces were slightly concave, with depths below 1 mm. (The interface depth is the axial location of the interface at the wall of the ampoule minus the axial location of the interface at the center).

It was observed that grains with orientations such that a {111} twin plane was approximately parallel to the growth direction were favored. If grains with these orientations happened to nucleate, they persisted along the entire ingot length. This was also observed in the $In_xGa_{1-x}Sb$ ingots grown by the gradient-freeze technique on earth and in space [25]. From observations of twinning in germanium and silicon, Billig [52] also suggested that having a {111} plane parallel to the main temperature gradient (perpendicular to the solid/melt interface) was a preferred condition for growth.

Capper et al. [15] found that application of ACRT with rotation rates of 30 to 60 rpm to the growth of $Cd_xHg_{1-x}Te$ ingots resulted in a reduction of the interface depth from 4 mm to below 1 mm. They found that fewer grains existed in ingots grown using ACRT rotation rates that resulted in more planar interfaces. Coates et al. [17] speculated that ACRT caused a reduction in the number of nuclei present in the melt ahead of the interface due to the enhanced heat and mass transfer caused by ACRT. It is more likely that the reduction in the concavity of the interface resulted in fewer grains nucleating at the wall of the ampoule and growing inward.

The results of the interface demarcation studies showed that application of ACRT using a rotation rate of 80 rpm to the solidification of $In_xGa_{1-x}Sb$ resulted in a reduction of the interface depth from 0.6 mm to 0.3 mm. If improvement in the grain selection due to a reduction in the concavity of the interface was the mechanism by which the number of grains was reduced in $Cd_xHg_{1-x}Te$, the reduction of the number of grains in $In_xGa_{1-x}Sb$ should have been much less. This is because the interface was extremely concave (4 mm deep) in ingots of $Cd_xHg_{1-x}Te$ solidified without ACRT [15]. More room for improvement existed. Application of ACRT reduced the interface depth from 4 mm to 1 mm [15]. Since the reduction in the number of grain boundaries in the ingots grown by Capper et al. was not assessed quantitatively, the reduction seen for $In_xGa_{1-x}Sb$ cannot be compared directly with the reduction for $Cd_xHg_{1-x}Te$. Also, Capper et al. investigated many more combinations of ACRT conditions to get the maximum improvement in grain structure. Qualitatively, it does seem that the reduction in the number of grains obtained by applying ACRT to the growth of $In_xGa_{1-x}Sb$ was not as great as that obtained for $Cd_xHg_{1-x}Te$.

Another possible explanation for the reduction in grain boundaries is that periodic meltback of the grown crystal results from ACRT. Larrousse and Wilcox [38,39] showed that strong, periodic fluctuations in mass transfer are caused by ACRT. Periodic fluctuations in heat transfer would also be present. This could lead to periodic meltback and regrowth. Jackson and Miller [40] showed the benefit of periodic melting and regrowth using the organic compound salol. They solidified salol in the hot-stage of a microscope. They observed the solidification behavior when cold blasts of liquid nitrogen were periodically blown onto the sample. The grain structure of the sample solidified with periodic melting and regrowth was improved. It was thought that defects melted back preferentially due to their higher energy.

Twin Boundaries. The fewest number of twin boundaries existed in ingots grown using ACRT rotation rates of 50 rpm and 80 rpm, with 80 rpm being the best. Ingots E1, E5, and E9 were solidified without using ACRT. Ingot E1 was the first ingot solidified and ingot E9 was the last. The difference in the number of twin boundaries in ingots E1 and E9 was found to be statistically insignificant. This suggests that the results are repeatable from ingot to ingot. However, ingot E5 had an unusually high number of twin boundaries. No reason for this is known. This ingot was ignored for the purpose of comparing the number of twin boundaries in ingots solidified using ACRT with that in ingots solidified without ACRT. Using an ACRT rotation rate of 80 rpm led to a 19% reduction in the number of twin boundaries.

As discussed in the preceding section on grain boundaries, grains whose orientation aligns a {111} twin plane with the growth direction (perpendicular to the solid/melt interface) seemed to be favored. If a grain with an orientation like this happened to nucleate, it persisted throughout the length of the ingot. Therefore, the shape of the solid/melt interface would control how rapidly these twins would grow out. With a concave interface, the twins would grow toward the center of the ingot and end when they met another grain or twin boundary. The intersection of boundaries can cause more grains and twins to form. The twins would persist for the entire ingot length when the interface was near planar, and they would grow into the wall of the ampoule if the interface was convex. This suggests that the number of twins remaining in the ingot can be changed by changing the interface shape. It was observed in ingots E1 to E9 that grains with twins at large angles to the growth direction never persisted for the entire length of the ingot. The twin boundaries grew out rapidly due to their angle with the wall of the ampoule and surrounding grains. Grains that were oriented such that the twins were parallel with the growth direction per-

sisted and had many twins. This was because every time a new twin nucleated it remained for the entire length of the ingot.

Twin boundaries in ingots of $In_xGa_{1-x}Sb$ grown by the gradient-freeze technique on earth and in space were found to have kinked or jogged in an attempt to align themselves perpendicular to the solid/melt interface [26]. This agrees with the suggestions that grains whose orientation aligns a twin plane parallel to the growth direction seem to be favored [25,52]. Kinking of twins was seen to a smaller extent in ingots E1 to E9. This means that the interface shape can influence the number of twin boundaries in the same way that it influences the number of grain boundaries.

The conclusion resulting from the preceding two paragraphs is that application of ACRT could have reduced the number of twin boundaries in the same way that it reduced the number of grain boundaries. Application of ACRT caused a reduction in the concavity of the interface. This led to improved grain selection and twin selection. However, the interface shape both with and without application of ACRT was slightly concave. It is not clear whether or not a significant change in grain and twin selection occurred with such a small change in interface shape. The number of twins was dramatically increased in grains with twin planes parallel to the growth direction. Perhaps, whether or not a grain with this orientation nucleated determined the number of twin boundaries in the ingot. Another possibility is that periodic melting and regrowth occurred and reduced the number of twin boundaries as was discussed for grain boundaries.

Interface Demarcation. Application of ACRT resulted in a reduction of the interface depth from 0.6 mm to 0.3 mm. (The interface depth is the axial location of the interface at the wall of the ampoule minus the axial location of the interface at the center). When ACRT is applied, strong, periodic mixing occurs above the interface [38,39]. An increase in the level of heat transfer would accompany this. It is possible that the increased heat transfer decreased the radial temperature gradients that existed in the melt next to the interface. This led to a more planar interface.

Conclusions

The axial composition profiles for ingots E1 to E6 suggest that these ingots were solidified from a well-mixed melt. This was true regardless of whether ACRT was applied or not. Analysis of the growth conditions suggests that diffusion may have been capable of completely mixing the melt. It is possible that the characteristic diffusion length D/V, where D is the diffusivity of InSb in the melt and V is the

solidification rate, was greater than the length of the entire ingot L.

No radial segregation was found in any of the ingots. The most significant conclusion from this is that application of ACRT did not create radial segregation in the ingots.

Application of ACRT using a rotation rate of 80 rpm and a cycle time of 10 s led to a reduction of the interface depth from 0.6 mm to 0.3 mm. (The interface depth is the axial location of the edge of the interface minus the axial location of the center).

Application of ACRT using a rotation rate of 80 rpm led to a consistent reduction in the number of twin boundaries and grain boundaries compared to ingots grown without ACRT. It is possible that the reduction in the number of grain and twin boundaries was due to better grain selection caused by a less concave interface. Even though a direct relationship between the interface shape and the grain structure has been demonstrated for $Cd_xHg_{1-x}Te$ [18] and $In_xGa_{1-x}Sb$, no cause-and-effect relationship has been established.

References

[1] J.C. McGroddy, M.R. Lorenz, and T.S. Plaskett, *Solid State Communications* **7** (1969) 901-903.

[2] T.S. Plaskett and J.F. Woods, *J. Crystal Growth* **11** (1971) 341-344.

[3] A. Joullie, J. Allegre, and G. Bougnot, *Mat. Res. Bull.* **7** (1972) 1101-1108.

[4] G.B. Blom and T.S. Plaskett, *J. Electrochem. Soc.* **118** (1971) 1831.

[5] W.A. Tiller, K.A. Jackson, J.W. Rutter, and B. Chalmers, *Acta Met.* **1** (1953) 428-437.

[6] J.W. Rutter and B. Chalmers, *Can. J. Phys.* **31** (1953) 15-39.

[7] W.W. Mullins and R.F. Sekerka, *J. Applied Phys.* **34** (1963) 323-329.

[8] W.W. Mullins and R.F. Sekerka, *J. Applied Phys.* **35** (1964) 444-453.

[9] R.F. Sekerka, *J. Applied Phys.* **36** (1965) 264-267.

[10] S. Sen, *PhD Thesis*, University of Southern California (1976).

[11] P. Capper, J.J.G. Gosney, and C.L. Jones, *J. Crystal Growth* **70** (1984) 356-364.

[12] J.C. Clayton, M.C. Davidson, D.C. Gillies, and S.L.Lehoczky, *J. Crystal Growth* **60** (1982) 374-380.

[13] P. Capper, C.L. Jones, E.J. Pearce, and M.J.T. Quelch, *J. Crystal Growth* **62** (1983) 487-497.

[14] B.E. Bartlett, P. Capper, J.E. Harris and M.J.T. Quelch, *J. Crystal Growth* **46** (1979) 623.

[15] P. Capper, W.G. Coates, C.L. Jones, J.J. Gosney, C.K. Ard, and I. Kenworthy, *J. Crystal Growth* **83** (1987) 69-76.

[16] P. Capper, J.C. Brice, C.L. Jones, W.G. Coates, J.J.G. Gosney, C. Ard, and I. Kenworthy, *J. Crystal Growth* **89** (1988) 171-176.

[17] W.G. Coates, P. Capper, C.L. Jones, J.J.G. Gosney, C.K. Ard, and I. Kenworthy, *J. Crystal Growth* **94** (1989) 959-966.

[18] P. Capper, W.G. Coates, C.L. Jones, J.J.G. Gosney, I. Kenworthy, and C.K. Ard, *J. Crystal Growth* **102** (1990) 848-856.

[19] F.R. Szofran and S.L. Lehoczky, *J. Crystal Growth* **70** (1984) 349.

[20] F.R. Szofran, D. Chandra, J.-C. Wang, E.K. Cothran, and S.L. Lehoczky, *J. Crystal Growth* **70** (1984) 343.

[21] R.N. Andrews, F.R. Szofran, and S.L. Lehoczky, *J. Crystal Growth* **92** (1988) 445-453.

[22] Ching-Hua Su, S.L. Lehoczky, and F.R. Szofran, *J. Crystal Growth* **86** (1988) 87-92.

[23] H. Potts and W.R. Wilcox, *J. Crystal Growth* **74** (1986) 443-445.

[24] J.F. Yee, M. Lin, K. Sarma, and W.R. Wilcox, *J. Crystal Growth* **30** (1975) 185-192.

[25] K. Sarma, *PhD Thesis*, University of Southern California (1976).

[26] R.A. Lefever, W.R. Wilcox, and K.R. Sarma, *Mat. Res. Bull.* **13** (1978) 1175-1180.

[27] J.F. Yee, S. Sen, K. Sarma, M. Lin, and W.R. Wilcox, *Proceedings - Third Space Processing Symposium - Skylab Results* **1** (1974).

[28] S. Sen, W.R. Wilcox, and R.A. Lefever, *Metallurgical Trans.* **9A** (1978) 462-464.

[29] H.P. Greenspan, *The Theory of Rotating Fluids*, Cambridge at the University Press (1968).

[30] E.R. Benton and A. Clark, Jr., *Ann. Rev. of Fluid Mech.* 6 (1974) 257-280.

[31] E.O. Schulz-DuBois, *J. Crystal Growth* 12 (1972) 81-87.

[32] H.J. Scheel and E.O. Schulz-DuBois, *J. Crystal Growth* 8 (1971) 304-306.

[33] H.J. Scheel, *J. Crystal Growth* 13-14 (1972) 560-565.

[34] A. Horowitz, D. Gazit, and J. Makovsky, *J. Crystal Growth* 61 (1983) 323-328.

[35] W. Tolksdorf and F. Welz, *Crystals - Growth, Properties, and Applications* Vol. 1, Springer-Verlag, Berlin-Heidelberg-New York (1978).

[36] D.H. Kim and R.A. Brown, *J. Crystal Growth* 96 (1989) 609-627.

[37] S. Durcok and E. Pollert, *J. Crystal Growth* 82 (1987) 501-508.

[38] M.F. Larrousse and W.R. Wilcox, *Chemical Eng. Science* 45 No. 6 (1990) 1571-1581.

[39] M.F. Larrousse, *PhD Thesis*, Clarkson University (1987).

[40] K.A. Jackson and C.E. Miller, *J. Crystal Growth* 42 (1977) 364-369.

[41] D.C. Gillies, *J. Elect. Mat.* Vol. II, No. 4 (1982) 689-697.

[42] J.C. Woolley and B.A. Smith, *Proc. Phys. Soc.* 72 (1958) 214-223.

[43] G.E.P. Box, W.G. Hunter, and J.S. Hunter, *Statistics for Experimenters*, John Wiley & Sons, Inc., New York (1978) 110-115,119-122.

[44] R.G.D. Steel and J.H. Torrie, *Principles and Procedures of STATISTICS*, McGraw-Hill Book Co., Inc., New York (1960) 78-81.

[45] L. Regel, *private communication* (1990).

[46] D. Camel and J.J. Favier, *J. Physique* 47 (1986) 1001-1014.

[47] P.M. Adornato and R.A. Brown, *J. Crystal Growth* 80 (1987) 155-190.

[48] B. Chalmers, *Can. J. Physics* 31 (1953) 132.

[49] D.T.J. Hurle, *Prog. Mat. Sci.* 10 (1962) 79.

[50] W.A. Tiller, *Principles of Solidification*, in: *The Art and Science of Growing Crystals*, Ed. J.J. Gilman, John Wiley & Sons, New York (1963) 276-312.

[51] J.C. Brice, *The Growth of Crystals from the Melt*, in: *Selected Topics in Solid State Physics*, Vol. V, Ed. E.P. Wohlfarth, John Wiley & Sons, New York (1965) 122-123.

[52] E. Billig, *J. Inst. Metals* 83 (1954-1955) 53.